

Consistency Regularised Gradient Flows for Inverse Problems

Alessio Spagnoletti^{1*} Tim Y. J. Wang^{2*}
 Marcelo Pereyra^{3†} O. Deniz Akyildiz^{2†}

¹Laboratoire MAP5, UMR 8145, Université Paris Cité, CNRS

²Department of Mathematics, Imperial College London

³Heriot-Watt University, MACS & Maxwell Institute

alessio.spagnoletti@etu.u-paris.fr tw1320@ic.ac.uk

M.Pereyra@hw.ac.uk deniz.akyildiz@imperial.ac.uk

*Joint first authors †Equal contribution

Abstract

Vision-Language Latent Diffusion Models (LDMs) [Rombach et al., 2022] provide powerful generative priors for inverse problems. However, existing LDM-based inverse solvers typically require a large number of neural function evaluations (NFEs) and backpropagation through large pretrained components, leading to substantial computational cost and, in some cases, degraded reconstruction quality. We propose a unified Euclidean-Wasserstein-2 gradient-flow framework that jointly performs posterior sampling and prompt optimization in the latent space through a single flow that aligns the prior and posterior with the observed data. Combined with few-step latent text-to-image models, this formulation enables low-NFE inference without backpropagation through autoencoders. Experiments across several canonical imaging inverse problems show that our method achieves state-of-the-art performance with significantly reduced computational cost.

1 Introduction

We consider methods for performing inference on a signal $\mathbf{x}_0 \in \mathbb{R}^n$ from a measurement

$$\mathbf{y} = \mathcal{A}(\mathbf{x}_0) + \mathbf{n}, \quad \mathbf{n} \sim \mathcal{N}(0, \sigma_y^2 I), \quad (1)$$

where $\mathcal{A} : \mathbb{R}^n \rightarrow \mathbb{R}^m$ is a known forward operator and \mathbf{n} is Gaussian noise. Such inverse problems can be effectively addressed in a Bayesian statistical framework [Stuart, 2010], where inference about \mathbf{x}_0 is based on the posterior distribution

$$p(\mathbf{x}_0 | \mathbf{y}) \propto p(\mathbf{y} | \mathbf{x}_0)p(\mathbf{x}_0).$$

Modern Bayesian imaging techniques increasingly rely on pretrained generative models as priors $p(\mathbf{x}_0)$, with a likelihood $p(\mathbf{y} | \mathbf{x})$ defined at test time. These so-called Plug & Play (PnP) zero-shot inference methods are a rapidly growing research area, as they require no task-specific fine-tuning and provide effective, general-purpose inverse solvers. Methods based on Diffusion Models (DMs) [Sohl-Dickstein et al., 2015, Song and Ermon, 2019, 2020,

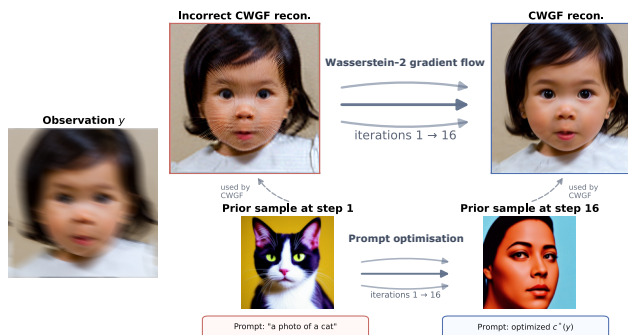


Figure 1: Our Euclidean-Wasserstein flow jointly optimizes the text prompt and yields accurate posterior samples in few NFEs. Zoom in for fine details.

Song et al., 2020b, Ho et al., 2020, 2022, Blattmann et al., 2023, Wan et al., 2025] are the current standard, with approaches such as DPS [Chung et al., 2023], DDRM [Kawar et al., 2022], DiffPIR [Zhu et al., 2023], IIGDM [Song et al., 2023a], and TMPD [Boys et al., 2024] for image restoration and [Kwon and Ye, 2025, Kwon et al., 2025] for video. More recently, Latent Diffusion Models (LDMs) [Rombach et al., 2021, Podell et al., 2023] have improved efficiency by operating in the latent space of a VAE rather than in pixel space [Kingma and Welling, 2013, Lopez et al., 2020]. However, because the likelihood is defined in pixel space, naively applying DM-based solvers to LDMs fails. Instead, the specific properties of the latent space need to be considered, as proposed in PSLD [Rout et al., 2023].

State-of-the-art results are achieved with vision-language LDMs such as Stable Diffusion [Rombach et al., 2021, Podell et al., 2023], which condition generation on semantic information via an (embedded) text prompt $c \in \mathbb{R}^d$ that must be carefully adjusted to the scene. Early methods tuned prompts heuristically (see, e.g., P2L [Chung et al., 2024] and TReg [Kim et al., 2025a]), while LATINO-PRO [Spagnoletti et al., 2025b] adopts an empirical Bayesian approach, estimating c by maximum marginal likelihood estimation (MMLE) $\hat{c}(\mathbf{y}) = \arg \max_{c \in \mathbb{R}^d} p_c(\mathbf{y})$.

However, leveraging vision-language LDMs for inverse problems is computationally demanding: naive solvers require hundreds of NFEs per posterior sample, and incorporating the likelihood $p(\mathbf{y} | \mathbf{x})$ requires evaluating (and possibly differentiating) the latent-to-pixel decoder model, substantially increasing memory footprint. Recent efforts to speed up sampling rely on distillation techniques, including direct distillation [Luhman and Luhman, 2021, Zheng et al., 2022], adversarial distillation [Wang et al., 2022, Sauer et al., 2023], and variational score distillation [Wang et al., 2023, Yin et al., 2024a,b, Luo et al., 2023c, Salimans et al., 2024]. In particular, Consistency Models (CMs) [Song et al., 2023b, Song and Dhariwal, 2023, Kim et al., 2023] have emerged as effective few-step generators, and their formulation enables both distillation from pre-trained DMs and training in isolation via consistency training (CT). CMs learn consistency functions that directly map noise to data, enabling accurate generation in few steps. Several recent works have explored CMs within a PnP sampling framework [Garber and Tirer, 2025, Xu et al., 2024, Li et al., 2025, Spagnoletti et al., 2025b,a], as well as fine-tuning models to sample directly from $p(\mathbf{x}|\mathbf{y})$, as done in CoSIGN [Zhao et al., 2024] or UD2M [Mbakam et al., 2025].

The state of the art in this context is LATINO-PRO, a CM-based method with automatic prompt tuning that avoids backpropagation through autoencoders. However, its stochastic approximation structure, which alternates sampling and prompt optimization steps, converges slowly and requires over 50 NFEs per sample. Instead, we pursue a unified approach that jointly samples and optimizes prompts in a single flow. Our contributions are as follows:

- We propose a novel Euclidean-Wasserstein gradient flow framework for inverse problems with LCMs. This leads to a fast, provably convergent method for joint posterior sampling and prompt optimization, requiring gradients only w.r.t. the prompt.
- Our method achieves SOTA performance in only 16 NFEs, significantly outperforming competing strategies, even under severely misspecified prompts.

2 Background

Notations. We use $\mathbf{X} = \mathbb{R}^n$ to denote the ambient (pixel) space, $\mathbf{Y} \subseteq \mathbb{R}^m$ the observation space, and $\mathbf{Z} = \mathbb{R}^l$ the latent space in which the prior is defined. We denote the space of probability measures on \mathbb{R}^d with finite q -th moments as $\mathcal{P}_q(\mathbb{R}^d)$; in this work, we focus on the case $q = 2$. We use $\delta\mathcal{F}[\mu]/\delta\mu$ to denote the first L^2 -variation of functional \mathcal{F} at μ .

Latent diffusion models. LDMs operate in the latent space of VAE $(\mathcal{E}_{\phi^-}, \mathcal{D}_{\phi^-})$ [Kingma and Welling, 2013, Rombach et al., 2022]. They are defined by a forward (noising) process on \mathbf{Z} that transports the clean embeddings $\mathbf{z}_0 \sim p_c(\mathbf{z}_0)$ to a reference distribution (e.g., $\mathcal{N}(0, I)$), and a corresponding reverse-time process that transports back to $p_c(\mathbf{z}_0)$, described by the SDEs [Sohl-Dickstein et al., 2015, Ho et al., 2020, Song et al., 2020b, Rombach et al., 2022]:

$$d\mathbf{z}_t = -\frac{\beta(t)}{2}\mathbf{z}_t dt + \sqrt{\beta(t)} d\mathbf{w} \quad d\mathbf{z}_t = \left(-\frac{\beta(t)}{2}\mathbf{z}_t - \beta(t)\nabla_{\mathbf{z}_t} \log p_{c,t}(\mathbf{z}_t)\right) dt + \sqrt{\beta(t)} d\bar{\mathbf{w}},$$

where the (intractable) score $\nabla_{\mathbf{z}_t} \log p_{c,t}(\mathbf{z}_t)$ controls the drift and $\beta(t)$ the transitions:

$$q(\mathbf{z}_t | \mathbf{z}_0) = \mathcal{N}(\mathbf{z}_t; \sqrt{\alpha_t} \mathbf{z}_0, \sigma_t^2 I), \quad \alpha_t = \exp\left(-\int_0^t \beta(s) ds\right), \quad \sigma_t^2 = 1 - \alpha_t. \quad (2)$$

In practice, the score is approximated by a neural network $s_{\theta,c}(\mathbf{z}_t, t) \approx \nabla_{\mathbf{z}_t} \log p_{c,t}(\mathbf{z}_t)$ via score matching [Vincent, 2011], and the reverse SDE is replaced by a *probability flow ODE* (PF-ODE) equivalent in marginals and more efficient to compute [Song et al., 2020b]:

$$\frac{d\mathbf{z}_t}{dt} = f(\mathbf{z}_t, t) - \frac{1}{2}g(t)^2 s_{\theta,c}(\mathbf{z}_t, t), \quad (3)$$

for suitable drift f and diffusion coefficient g (e.g., in the Variance Preserving (VP) case, $f(\mathbf{z}_t, t) = -\frac{1}{2}\beta(t)\mathbf{z}_t$ and $g(t) = \sqrt{\beta(t)}$ [Ho et al., 2020, Song et al., 2020b]).

Consistency models. CMs enable few-step generation by replacing iterative SDE/ODE sampling with a learned *consistency function* that maps a noisy state at time t directly to a clean sample by transporting along PF-ODE trajectories [Song et al., 2023b, Song and Dhariwal, 2023]. LCMs use a prompt-conditioned consistency function $g_\theta : (\mathbf{z}_t, t, c) \mapsto \hat{\mathbf{z}}_0$ that predicts the clean embedding on the trajectory. Informally, for any $\{\mathbf{z}_t\}_{t \in [\eta, T]}$, we have

$$g_\theta(\mathbf{z}_t, t, c) = g_\theta(\mathbf{z}_{t'}, t', c) \quad \forall t, t' \in [\eta, T]. \quad (4)$$

CMs can be trained in isolation or by distilling a pretrained diffusion model, and can achieve excellent quality in as few as 4 – 8 NFEs [Song et al., 2023b, Yin et al., 2024a,b].

At inference, given a decreasing time sequence $T = t_0 > t_1 > \dots > t_{K-1} > \eta$ and a purely noisy sample $\hat{\mathbf{z}}_{t_0} \sim \mathcal{N}(0, I)$, multistep CM sampling alternates between (i) denoising with g_θ and (ii) re-noising to the next time point via the noising process (2) [Song et al., 2023b]:

$$\hat{\mathbf{z}}_0 \leftarrow g_\theta(\hat{\mathbf{z}}_{t_k}, t_k, c), \quad (5)$$

$$\hat{\mathbf{z}}_{t_{k+1}} \leftarrow \sqrt{\alpha_{t_{k+1}}} \hat{\mathbf{z}}_0 + \sigma_{t_{k+1}} \varepsilon, \quad \varepsilon \sim \mathcal{N}(0, I). \quad (6)$$

This “denoise–renoise” recursion underlies Latent Consistency Models (LCMs) as fast priors for inverse problems. In practice, LCMs are typically distilled from Stable Diffusion LDMs in latent space [Rombach et al., 2022, Luo et al., 2023a], often using lightweight adapters such as LoRA [Hu et al., 2022, Luo et al., 2023b].

3 A Euclidean-Wasserstein Gradient Flow Approach

Our proposed Consistency-regularised Wasserstein Gradient Flow (CWGF) simultaneously optimises the prompt embedding by maximum marginal likelihood estimation and computes the associated empirical Bayesian posterior via a Wasserstein-2 gradient flow in latent space. We formulate our method as a continuous-time gradient flow over probability distributions and text embeddings, and derive efficient discretisations through an LCM in VAE latent space.

Bayesian model. Recall that we seek to perform inference on $\mathbf{x} \in \mathbf{X}$ from an observation $\mathbf{y} = \mathcal{A}(\mathbf{x}) + \epsilon$, where $\mathcal{A} : \mathbf{X} \rightarrow \mathbf{Y}$ is a known linear operator and $\epsilon \sim \mathcal{N}(0, \sigma_{\mathbf{y}}^2 I)$ is measurement noise. We further assume that \mathbf{x} is generated from a latent variable $\mathbf{z} \in \mathbf{Z}$ via a pretrained VAE decoder $p_{\phi^-}(\mathbf{x}|\mathbf{z})$. The prior on \mathbf{z} is parametrised by a text prompt embedding $c \in \mathbf{C}$ encoded by a CM $p_c(\mathbf{z})$ [Luo et al., 2023a, Yin et al., 2024a]. From Bayes’ theorem:

$$p_c(\mathbf{x}, \mathbf{z}|\mathbf{y}) = \frac{p(\mathbf{y}|\mathbf{x})p_{\phi^-}(\mathbf{x}|\mathbf{z})p_c(\mathbf{z})}{p_c(\mathbf{y})}, \quad (7)$$

with data likelihood $p(\mathbf{y}|\mathbf{x}) := \mathcal{N}(\mathbf{y}; \mathcal{A}(\mathbf{x}), \sigma_{\mathbf{y}}^2 I)$ and where $p_c(\mathbf{y})$ is the marginal likelihood of c .

Optimisation objective in $\mathbf{C} \times \mathcal{P}_2(\mathbf{Z})$. Our method seeks to solve optimisation problems defined on the product space $\mathbf{C} \times \mathcal{P}_2(\mathbf{Z})$, where \mathbf{C} is the prompt embedding space and $\mathcal{P}_2(\mathbf{Z})$ the space of probability measures on the latent space \mathbf{Z} with finite second moment. We consider optimisation problems of the form:

$$(c_\star, \mu_\star) = \arg \min_{(c, \mu) \in \mathbf{C} \times \mathcal{P}_2(\mathbf{Z})} \mathcal{F}[c, \mu] := \mathcal{R}[c, \mu] + \mathcal{L}[\mu], \quad (8)$$

where \mathcal{R} and \mathcal{L} are functionals defined on $\mathbb{C} \times \mathcal{P}_2(\mathbb{Z})$ and $\mathcal{P}_2(\mathbb{Z})$ respectively. While this formulation (hence our method) can be quite general, we focus on the case where \mathcal{R} and \mathcal{L} are the KL divergence and negative log-likelihood respectively:

$$\mathcal{R}[c, \mu] = D_{\text{KL}}(\mu \| p_c), \quad \mathcal{L}[\mu] := -\mathbb{E}_\mu[\log p(\mathbf{y}|\mathbf{z})], \quad (9)$$

with \mathcal{R} being a regularisation term encouraging the latent distribution μ to be close to the CM-induced prior p_c , and $\mathcal{L}[\mu]$ being the negative log-likelihood term that matches the observed data \mathbf{y} through $p(\mathbf{y}|\mathbf{z}) := \int p(\mathbf{y}|\mathbf{x})p_{\phi^-}(\mathbf{x}|\mathbf{z})d\mathbf{x}$. This specific choice of \mathcal{R} and \mathcal{L} leads to empirical Bayesian inference with MMLE [Dempster et al., 1977] for the model in (7), i.e., to find $c_* \in \arg \max_{c \in \mathbb{C}} \log p_c(\mathbf{y})$, where $p_c(\mathbf{y}) := \int p_c(\mathbf{x}, \mathbf{y}, \mathbf{z})d\mathbf{x}d\mathbf{z}$ [Kuntz et al., 2023] and $\mu_* = p_{c_*}(\mathbf{z}|\mathbf{y})$. However, our framework can be applied to other choices of \mathcal{R} and \mathcal{L} , such as those arising from generalised Bayesian inference [Bissiri et al., 2016].

A Gradient Flow in $\mathbb{C} \times \mathcal{P}_2(\mathbb{Z})$. Similar to how gradient flow $\dot{x}_\tau = -\nabla f(x_\tau)$ in \mathbb{R}^d minimises a function $f : \mathbb{R}^d \rightarrow \mathbb{R}$ in the Euclidean space, we seek an analogue of this flow applicable to $\mathcal{F}[c, \mu]$, which features gradients obtained by endowing \mathbb{C} with the Euclidean geometry and $\mathcal{P}_2(\mathbb{Z})$ with the Wasserstein-2 one (cf. Kuntz et al. [2023] and Appendix A.1):

$$\begin{cases} \dot{c}_\tau = -\nabla_c \mathcal{R}[c_\tau, \mu_\tau] \\ \dot{\mu}_\tau = -\text{grad}_{W_2} \mathcal{R}[c_\tau, \mu_\tau] - \text{grad}_{W_2} \mathcal{L}[\mu_\tau]. \end{cases} \quad (10)$$

where $\text{grad}_{W_2} \mathcal{F}$ is the Wasserstein-2 (W_2) gradient of a functional \mathcal{F} [Figalli and Glaudo, 2021, Chapter 4] defined via the first variation [Santambrogio, 2015, Section 7.2]: $\text{grad}_{W_2} \mathcal{F}[\mu](\mathbf{z}) = -\nabla \cdot (\mu \nabla_{\mathbf{z}} (\delta \mathcal{F} / \delta \mu)(\mathbf{z}))$. Along the flow (c_τ, μ_τ) , the value of $\mathcal{F}[c_\tau, \mu_\tau]$ is non-increasing and we recover the optimal solution (c_*, μ_*) at stationarity [Kuntz et al., 2023, Theorem 2] (cf. Appendix A.2 for the proof).

Theorem 1 (Optimality Conditions). *Under the loss (9), the gradient $\nabla \mathcal{F}[c, \mu] := (\nabla_c \mathcal{R}[c, \mu], \text{grad}_{W_2} \mathcal{F}[c, \mu])$ vanishes if and only if we attain the posterior $\mu = p_{c_*}(\mathbf{z}|\mathbf{y})$ and the marginal likelihood stationary point $\nabla_c \log p_c(\mathbf{y}) = 0$, where $p_c(\mathbf{y}) = \int p_c(\mathbf{x}, \mathbf{y}, \mathbf{z})d\mathbf{x}d\mathbf{z}$.*

This shows that the objective \mathcal{F} in (9) recovers the optimal prompt c^* and posterior μ^* in latent space, matching the MMLE solution of (7). Under mild conditions (e.g., strong log-concavity of $p_c(\mathbf{y}, \mathbf{z})$), the flow converges exponentially fast to (c^*, μ^*) (see Appendix A.3).

We now discretize the flow in time and space, yielding a fast algorithm for computing (c_*, μ_*) .

Time Discretisation of the Gradient Flow (10)-(11). As a first step to convert eqs. (10) and (11) into an implementable algorithm, we write out the time-discretised version of the flow in this section. The main challenge in discretising the flow is the structure of the Wasserstein gradient in (11). To address this, we exploit the additive composition of the W_2 gradient in (11) and consider a Lie-Trotter splitting of the gradient flow similar to those in Clément and Maas [2011], Wibisono [2018], Bernton [2018]. Together with the prompt update in (10), we obtain the following splitting scheme for the flow where one-step updates are performed sequentially for the prompt and the distribution:

$$\begin{cases} c_{\tau+h} = c_\tau - h \nabla_c \mathcal{R}[c_\tau, \mu_\tau] \\ \bar{\mu}_{\tau+h} = S_h^{\mathcal{R}, c_\tau} \mu_\tau \\ \mu_{\tau+h} = S_h^{\mathcal{L}} \bar{\mu}_{\tau+h}. \end{cases} \quad (12)$$

where $S_t^{\mathcal{R}, c_\tau}$ and $S_t^{\mathcal{L}}$ are the semigroups associated with the Wasserstein gradient subflows of \mathcal{R} and \mathcal{L} respectively in (11) with the prompt c_τ fixed. Under standard regularity assumptions, each subflow admits a Lagrangian representation via characteristics [Ambrosio et al., 2008, Chapter 8]: $\dot{z}_\tau = -\nabla_{\mathbf{z}} (\delta \mathcal{G} / \delta \mu)(z_\tau)$, where $z_\tau \sim \mu_\tau$ for all $\tau \geq 0$ and $\mathcal{G} \in \{\mathcal{R}, \mathcal{L}\}$. However, updates (12)–(14) are still idealised. In order to implement these updates, we next look at efficient spatial discretisations for the two subflows.

3.1 The prior subflow: kernelised entropy and CM-induced prior score

We now make the \mathcal{R} -subflow in (13) explicit. To spatially discretise the flow of $\mathcal{R}[c, \mu] = D_{\text{KL}}(\mu \| p_c)$, we need to compute the velocity field $-\nabla \delta \mathcal{R} / \delta \mu$ (cf. Lemma 1)

$$-\nabla_{\mathbf{z}} \frac{\delta \mathcal{R}}{\delta \mu}(\mathbf{z}) = \nabla_{\mathbf{z}} \log p_c(\mathbf{z}) - \nabla_{\mathbf{z}} \log \mu(\mathbf{z}). \quad (15)$$

Direct simulation via (15) is often infeasible, as $\mu^N(d\mathbf{z}) := N^{-1} \sum_n \delta_{\mathbf{z}^{(n)}}(d\mathbf{z})$ is an empirical measure and $\nabla \log p_c(\mathbf{z})$ can be ill-defined in high dimensions [Song and Ermon, 2019]. Instead, we consider approximating both $\nabla \log \mu$ and $\nabla \log p_c$ with a convex average of scores along the diffusion path. To this end, we first define the diffusion path for both p_c and μ under the VP schedule $\dot{\alpha}_t = -\beta_t \alpha_t$ (2), with $\alpha_t \in (0, 1]$ and $\sigma_t^2 = 1 - \alpha_t$:

$$p_{c,t} := Q_t * p_c, \quad \mu_t := Q_t * \mu, \quad (Q_t * \mu)(\mathbf{z}_t) := \int q(\mathbf{z}_t | \mathbf{z}_0) \mu(\mathbf{z}_0) d\mathbf{z}_0, \quad (16)$$

where $q(\mathbf{z}_t | \mathbf{z}_0) = \mathcal{N}(\mathbf{z}_t; \sqrt{\alpha_t} \mathbf{z}_0, \sigma_t^2 \mathbf{I})$. For $r \in \{\mu, p_c\}$, the marginals $r_t := Q_t * r$ are equal to the laws of the particles following the probability-flow ODEs $\dot{\mathbf{z}}_s^r = -(\beta_s/2)(\mathbf{z}_s^r + \nabla \log r_s(\mathbf{z}_s^r; c))$, where $t \in [0, T]$ and $\mathbf{z}_t^r = \mathbf{z}_t \sim r_t$. Denoting $G_t^r(\mathbf{z}_t) := \mathbf{z}_0^r$ as the flow map obtained by integrating the PF-ODE (3) from time t to 0, we have the following exact identity (proved in Appendix A.4).

Proposition 1 (Exact flow-map identity). *For every $t > 0$ and $s \in [0, t]$, we have for any law $r \in \mathcal{P}_2(\mathbf{Z})$, and $\mathbf{z}_t \sim r_t(\mathbf{z}_t)$*

$$\frac{\sqrt{\alpha_t} G_t^r(\mathbf{z}_t) - \mathbf{z}_t}{1 - \sqrt{\alpha_t}} = \int_0^t \gamma_t(s) \nabla_{\mathbf{z}_s^r} \log r_s(\mathbf{z}_s^r) ds, \quad \gamma_t(s) := \frac{\sqrt{\alpha_t}}{1 + \sqrt{\alpha_t}} \frac{\beta_s}{2\sqrt{\alpha_s}}, \quad (17)$$

where $\gamma_t(s) \geq 0$ and $\int_0^t \gamma_t(s) ds = 1$. In particular, this convex average of scores approximates $\nabla \log r(\mathbf{z}_0^r)$ accurately at small t (cf. Appendix B for a discussion).

Proposition 1 implies that we can approximate the intractable drift (15) by a flow-map discrepancy that can be evaluated by a CM

$$-\nabla_{\mathbf{z}} \frac{\delta \mathcal{R}}{\delta \mu}(\mathbf{z}) := \frac{\sqrt{\alpha_t}}{1 - \sqrt{\alpha_t}} (G_t^{p_c}(\mathbf{z}_t) - G_t^{\mu}(\mathbf{z}_t)) \approx \nabla_{\mathbf{z}} \log p_c(\mathbf{z}) - \nabla_{\mathbf{z}} \log \mu(\mathbf{z}). \quad (18)$$

The prior origin map $G_t^{p_c}$ is approximated by the consistency model $g_{\theta}(\mathbf{z}_t, t, c)$. For the current particle law μ^N , we approximate the map $G_t^{\mu^N}$ by the denoiser under the VP forward kernel $\mathbb{E}_{\mu}[\mathbf{z}_0 | \mathbf{z}_t] \approx \widehat{m}_t^{\mu, N}(\mathbf{z}_t) = \sum_{m=1}^N \pi_m(\mathbf{z}_t; t) \mathbf{z}_0^{(m)}$ with $\pi_m(\mathbf{z}_t; t) \propto q(\mathbf{z}_t | \mathbf{z}_0^{(m)})$. Such an approximation has a bias of $\mathcal{O}(t)$ for small t [Kim et al., 2023]. Absorbing the factor $\sqrt{\alpha_t}/(1 - \sqrt{\alpha_t})$ into the step size η_t , we obtain the practical update

$$\mathbf{z}_{0,+}^{(n)} = \mathbf{z}_0^{(n)} + \eta_t \left(g_{\theta}(\mathbf{z}_t^{(n)}, t, c) - \mathbf{z}_0^{(n)} \right) + \eta_t \left(\mathbf{z}_0^{(n)} - \sum_{m=1}^N \pi_{nm}(t) \mathbf{z}_0^{(m)} \right), \quad (19)$$

where $\pi_{nm}(t) := \pi_m(\mathbf{z}_t^{(n)}; t)$ is the weight of the m -th particle in the denoiser estimate. The first two terms form a relaxation toward the CM output, while the final term is a kernelized repulsion away from the local barycentre of neighboring particles.

3.2 A Score-Based Prompt Flow

To jointly optimise the prompt c , we need to compute the gradient $\nabla_c D_{\text{KL}}(\mu \| p_c)$ to implement (12). Directly differentiating this KL divergence through the prior density $p_c(\mathbf{z})$ would require expensive simulation of the reverse SDE/ODE [Song et al., 2021b, Skreta et al., 2025]. Instead, under the same VP noising path as in the prior subflow and applying Song et al. [2021a, Theorem 2] gives the equivalent KL representation

$$D_{\text{KL}}(\mu \| p_c) = \frac{1}{2} \int_0^T \beta(t) D_{\text{F}}(\mu_t \| p_{c,t}) dt + D_{\text{KL}}(\mu_T \| p_{c,T}), \quad (20)$$

where T is the terminal diffusion time of the schedule in (2) and we denote the Fisher divergence as $D_{\text{F}}(\mu \| \nu) := \mathbb{E}_{\mu}[\|\nabla \log \mu(\mathbf{z}) - \nabla \log \nu(\mathbf{z})\|_2^2]$ with $\mu_t = Q_t * \mu$. Moreover, using denoising score matching [Vincent, 2011, Song and Ermon, 2019] and assuming the terminal mismatch $D_{\text{KL}}(\mu_T \| p_{c,T})$ is negligible, we can estimate the gradient with

$$\nabla_c D_{\text{KL}}(\mu \| p_c) = \frac{1}{2} \nabla_c \int_0^T \beta(t) \mathbb{E}_{\mathbf{z}_0 \sim \mu} \mathbb{E}_{\mathbf{z}_t \sim q_t(\cdot | \mathbf{z}_0)} [\|\nabla_{\mathbf{z}_t} \log q(\mathbf{z}_t | \mathbf{z}_0) - s_{\theta}(\mathbf{z}_t, t; c)\|_2^2] dt, \quad (21)$$

which is approximated using Monte-Carlo in practice. To evaluate the scores s_θ , we use the score output from the LCM as a proxy by reparametrising $s_\theta(\mathbf{z}, t; c) = -\sigma_t^{-1}\hat{\epsilon}_\theta(\mathbf{z}, t; c)$. Since the LCM is initialised from the diffusion model teacher [Song et al., 2023b, Luo et al., 2023a], it can often provide good surrogates for score estimates (we refer to Appendix G.6 for a more detailed discussion). Our method is also directly applicable to Consistency Trajectory Models (CTM) [Kim et al., 2023], which directly output score predictions.

3.3 An Encoder-based Likelihood Flow

We now consider the spatial discretisation of the flow of the likelihood part $\mathcal{L}[\mu] = -\mathbb{E}_\mu[\log p_{\phi^-}(\mathbf{y}|\mathbf{z})]$ in (14). A standard calculation yields $\delta\mathcal{L}/\delta\mu(\mathbf{z}) = -\log p(\mathbf{y}|\mathbf{z})$ (cf. Lemma 2). Thus, the drift of the likelihood descent subflow is $-\nabla_{\mathbf{z}}\delta\mathcal{L}/\delta\mu(\mathbf{z}) = \nabla_{\mathbf{z}}\log p(\mathbf{y}|\mathbf{z})$. Using Fisher’s identity to exchange the order of differentiation and integration, we can express this drift as

$$g(\mathbf{z}; \mathbf{y}) := \nabla_{\mathbf{z}} \log p(\mathbf{y}|\mathbf{z}) = \mathbb{E}_{p_c(\mathbf{x}|\mathbf{z}, \mathbf{y})}[\nabla_{\mathbf{z}} \log p_{\phi^-}(\mathbf{x}|\mathbf{z})]. \quad (22)$$

However, computing (22) would require backpropagating through the decoder, incurring high memory usage and potential artefacts [Raphaelli et al., 2025]. Instead, we exploit the encoder $q_{\phi^-}(\mathbf{z}|\mathbf{x})$ in the pretrained latent CM to obtain an approximation for $\nabla_{\mathbf{z}} \log p(\mathbf{x}|\mathbf{z})$ as illustrated in the following proposition (proved in Appendix A.5).

Proposition 2. *For a VAE trained with the objective $\mathcal{L}_{\text{VAE}}(\phi) = \mathbb{E}_{q_\phi}[-\log p_\phi(\mathbf{x}|\mathbf{z})] + \lambda D_{\text{KL}}(q_\phi(\mathbf{z}|\mathbf{x})||p_0(\mathbf{z}))$ with $\lambda > 0$ and $p_0(\mathbf{z})$ being a standard Gaussian, we have the approximation to (22) as:*

$$\hat{g}(\mathbf{z}; \mathbf{y}) := \lambda \int [\nabla_{\mathbf{z}} \log q_\phi(\mathbf{z}|\mathbf{x})] p_c(\mathbf{x}|\mathbf{z}, \mathbf{y}) d\mathbf{x} - \lambda \nabla_{\mathbf{z}} \log p_0(\mathbf{z}). \quad (23)$$

Furthermore, the error of approximation $\varepsilon(\hat{g}) := \|g(\mathbf{z}; \mathbf{y}) - \hat{g}(\mathbf{z}; \mathbf{y})\|_2^2$ satisfies $\varepsilon(\hat{g}) \leq \lambda^2 \mathbb{E}[\|\nabla_{\mathbf{z}} \log q^*(\mathbf{z}|\mathbf{x}) - \nabla_{\mathbf{z}} \log q_\phi(\mathbf{z}|\mathbf{x})\|_2^2]$, where $q^*(\mathbf{z}|\mathbf{x}) \propto p_0(\mathbf{z}) \exp(\lambda^{-1} \log p_\phi(\mathbf{x}|\mathbf{z}))$ is the optimal encoder distribution for the VAE objective and the expectation is over $p_c(\mathbf{x}|\mathbf{z}, \mathbf{y})$.

We point out that VAEs in the latent CMs are often trained with a small $\lambda \approx 10^{-4}$ [Rombach et al., 2022, Appendix G] and the encoder approximation error is often small for a well-trained VAE. To form a Monte Carlo/maximum a posteriori (MAP) estimate of the integral in (23), we require the pixel space posterior $p_c(\mathbf{x}|\mathbf{z}, \mathbf{y})$. In the specific case of linear inverse problems $p(\mathbf{y}|\mathbf{x}) = \mathcal{N}(\mathbf{y}; A\mathbf{x}, \sigma_{\mathbf{y}}^2 I)$ and Gaussian decoder $p_{\phi^-}(\mathbf{x}|\mathbf{z}) = \mathcal{N}(\mathbf{x}; \mathcal{D}_{\phi^-}(\mathbf{z}), \sigma_{\text{dec}}^2 I)$, the posterior $p_c(\mathbf{x}|\mathbf{z}, \mathbf{y}) = \mathcal{N}(\mathbf{x}; m(\mathbf{z}), \Sigma)$ is also Gaussian (cf. Appendix A.6) with $m(\mathbf{z})$ and Σ given by:

$$m(\mathbf{z}) = \Sigma (\sigma_{\text{dec}}^{-2} \mathcal{D}_{\phi^-}(\mathbf{z}) + \sigma_{\mathbf{y}}^{-2} A^\top \mathbf{y}), \quad \Sigma = (\sigma_{\text{dec}}^{-2} I + \sigma_{\mathbf{y}}^{-2} A^\top A)^{-1}. \quad (24)$$

Therefore, under the MAP approximation, the flow of \mathcal{L} in (14) admits the following approximate particle drift:

$$\dot{\mathbf{z}}_\tau = -\nabla_{\mathbf{z}} \frac{\delta\mathcal{L}}{\delta\mu}(\mathbf{z}_\tau) := \lambda \Sigma_{\phi^-}^{-1} (\mathcal{E}_{\phi^-}(m(\mathbf{z}_\tau)) - \mathbf{z}_\tau) + \lambda \mathbf{z}_\tau, \quad (25)$$

where we have used that the prior and encoder have diagonal Gaussian forms, *i.e.* $p_0(\mathbf{z}) = \mathcal{N}(\mathbf{z}; 0, I)$ and $q_{\phi^-}(\mathbf{z}|\mathbf{x}) = \mathcal{N}(\mathbf{z}; \mathcal{E}_{\phi^-}(\mathbf{x}), \Sigma_{\phi^-}(\mathbf{x}))$. We point out that (25) does not require backpropagation through either the CM or the VAE components. Concurrent to our work, Shtanchaev et al. [2026] also derived a similar objective for the likelihood gradient, albeit using heuristic arguments. We summarise the updates in Algorithm 1.

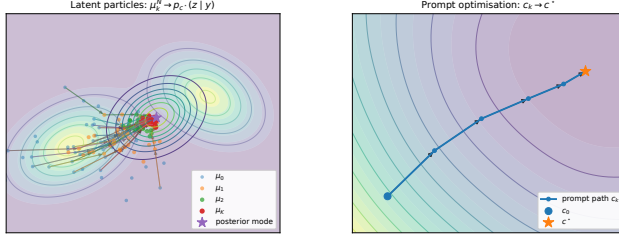


Figure 2: Schematic view of CWGF. The particle distribution μ_k^N is transported toward the posterior $p_{c^*}(\mathbf{z}|\mathbf{y})$, while the prompt embedding c_k is updated toward the marginal-likelihood optimum c^* .

4 Experiments

Datasets and prior model. We evaluate our method on two high-quality datasets at resolution 512×512 : FFHQ [Karras et al., 2019] and ImageNet [Deng et al., 2009]. For FFHQ, we use the first 1k test images, as in Chung et al. [2023]; for ImageNet, we use the *val1k* validation set introduced by Larsson et al. [2016]. Our prior is the LCM-LoRA [Luo et al., 2023b] distilled from Stable Diffusion 1.5. This is the same latent diffusion backbone used to evaluate diffusion-based baselines such as P2L [Chung et al., 2024], PSDL [Rout et al., 2023], LDPS, and LATINO/LATINO-PRO [Spagnoletti et al., 2025b].

Inverse problems. We consider the standard linear degradations used in Chung et al. [2023]. For Gaussian deblurring, we use a 61×61 kernel with $\sigma = 3.0$. For motion deblurring, we use a 61×61 kernel randomly sampled with intensity 0.5^1 . For super-resolution, we evaluate $\times 8$ upscaling with bicubic interpolation. In all experiments, the measurements are corrupted with additive white Gaussian noise of standard deviation $\sigma_{\mathbf{y}} = 0.01$. Additional results on nonlinear inverse problems are reported in Appendix F.

Implementation details. We discretise the proposed gradient-flow dynamics with explicit Euler steps. Following the coarse-to-fine nature of diffusion sampling [Wang et al., 2023], we use a two-stage timestep schedule for the prior flow: during the first half of the algorithm we traverse the full LCM timestep set $\{999, 879, 759, 639, 499, 379, 259, 139\}$, while during the second half we cycle through the four lowest-noise timesteps to refine high-frequency details. We run CWGF for 16 iterations. Since prompt and particle variables evolve on different scales [Pavliotis and Stuart, 2008, Akyildiz et al., 2024], we use separate stepsizes for the prompt and particle updates, and precondition the likelihood gradient by $\lambda^{-1}\Sigma_{\phi^-}$; see eq. (25). Full pseudo-code is given in Appendix C.

Results. Table 1 reports quantitative results on the selected inverse problems, while qualitative results are shown in Figure 5 for ImageNet, and in Figure 4 for FFHQ. All results are obtained with only $N = 1$ particle. In Appendix G, we report results with $N > 1$, for which we observe mild improvements compared to the case $N = 1$, as the high dimensionality of the latent space weakens the interactions. The results change when we run the algorithm on low-dimensional problems using the MNIST dataset Deng [2012], where particle interactions are important. Indeed, as shown in Figure 3, where the problem solved was inpainting, the distribution of the particles exhibits greater variability when sampled *all at once* (i.e., with $N > 1$) than in the *batched* case (i.e., in parallel with $N = 1$). A more detailed analysis of this setting is discussed in Appendix E.

Algorithm 1. Consistency-regularised Wasserstein Gradient Flow (CWGF)

- 1: **Inputs:** \mathbf{y} , particles $\{\mathbf{z}_0^{(n)}\}_{n=1}^N$, prompt c_0
 - 2: **for** $k = 0, \dots, K - 1$ **do**
 - 3: Sample $t = t(k)$ and $\varepsilon^{(n)} \sim \mathcal{N}(0, I)$
 - 4: $\mathbf{z}_t^{(n)} \leftarrow \sqrt{\alpha_t} \mathbf{z}_k^{(n)} + \sigma_t \varepsilon^{(n)}$
 - 5: $c_{k+1} \leftarrow c_k - \eta_c \nabla_{c_t} \mathcal{R}$ (21)
 - 6: $\pi_{nm}(t) \propto q(\mathbf{z}_t^{(n)} | \mathbf{z}_k^{(m)})$,
 - 7: $\widehat{m}_t^{\mu, N}(\mathbf{z}_t^{(n)}) \leftarrow \sum_m \pi_{nm}(t) \mathbf{z}_k^{(m)}$
 - 8: $\bar{\mathbf{z}}_k^{(n)} \leftarrow \mathbf{z}_k^{(n)} + \eta_R \left(g_{\theta}(\mathbf{z}_t^{(n)}, t, c_k) - \mathbf{z}_k^{(n)} \right) + \eta_R \left(\mathbf{z}_k^{(n)} - \widehat{m}_t^{\mu, N}(\mathbf{z}_t^{(n)}) \right)$ (19)
 - 9: Compute $m(\bar{\mathbf{z}}_k^{(n)})$ as in (24)
 - 10: $\widehat{g}(\bar{\mathbf{z}}_k^{(n)}; \mathbf{y}) \leftarrow \lambda \Sigma_{\phi^-}^{-1} \left(\mathcal{E}_{\phi^-}(m(\bar{\mathbf{z}}_k^{(n)})) - \bar{\mathbf{z}}_k^{(n)} \right) + \lambda \bar{\mathbf{z}}_k^{(n)}$ (25)
 - 11: $\mathbf{z}_{k+1}^{(n)} \leftarrow \bar{\mathbf{z}}_k^{(n)} + \eta_L \widehat{g}(\bar{\mathbf{z}}_k^{(n)}; \mathbf{y})$
 - 12: **end for**
 - 13: **Outputs:** $\{\mathcal{D}_{\phi^-}(\mathbf{z}_K^{(n)})\}_{n=1}^N, c_K$
-

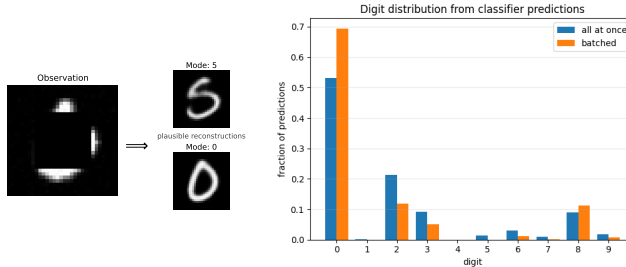


Figure 3: Distribution of digits among the samples.

¹<https://github.com/LeviBorodenko/motionblur>

Method	Gaussian Deblur				Motion Deblur			SR $\times 8$		
	NFE \downarrow	FID \downarrow	PSNR \uparrow	LPIPS \downarrow	FID \downarrow	PSNR \uparrow	LPIPS \downarrow	FID \downarrow	PSNR \uparrow	LPIPS \downarrow
FFHQ-512	Prompt: a photo of a face									
LATINO	8	40.01	26.27	0.352	35.36	25.19	0.405	50.34	25.25	0.444
LATINO-PRO	65	<u>32.48</u>	<u>28.49</u>	<u>0.325</u>	39.72	25.16	0.410	75.97	<u>26.00</u>	0.445
P2L	400	45.12	26.47	0.433	55.73	23.92	0.503	52.14	23.76	0.485
TReg	200	48.73	24.27	0.418	44.97	22.82	0.432	62.40	22.68	0.460
PSLD	200	128.79	17.15	0.595	173.6	15.81	0.629	61.90	23.19	0.535
LDPS	200	173.37	15.12	0.644	219.26	14.19	0.670	50.52	23.89	0.491
CWGF	<u>16</u>	21.95	29.42	0.309	23.18	27.98	0.338	37.37	27.07	0.366
ImageNet-512	Prompt: a photo in high resolution									
LATINO	8	52.95	23.43	0.406	53.49	22.29	0.468	73.90	22.53	0.502
LATINO-PRO	65	<u>35.18</u>	<u>25.28</u>	0.357	67.44	<u>22.51</u>	0.478	68.89	<u>23.06</u>	0.498
P2L	400	59.77	23.05	0.487	159.32	14.29	0.683	<u>55.04</u>	<u>22.56</u>	<u>0.468</u>
TReg	200	56.54	22.38	0.441	78.75	20.99	0.501	75.91	20.85	0.504
PSLD	200	129.8	15.43	0.615	152.9	14.15	0.645	129.8	15.43	0.615
LDPS	1000	152.0	13.81	0.649	166.8	13.05	0.667	105.3	20.32	0.610
CWGF	<u>16</u>	28.19	25.40	<u>0.394</u>	41.81	23.86	0.409	48.66	23.40	0.458

Table 1: Results for Gaussian deblurring with $\sigma = 3.0$, motion deblurring, and $\times 8$ super-resolution, all with measurement noise $\sigma_y = 0.01$, on FFHQ-512 and ImageNet-512 validation datasets. **Bold**: best within each dataset/problem; underline: second best.

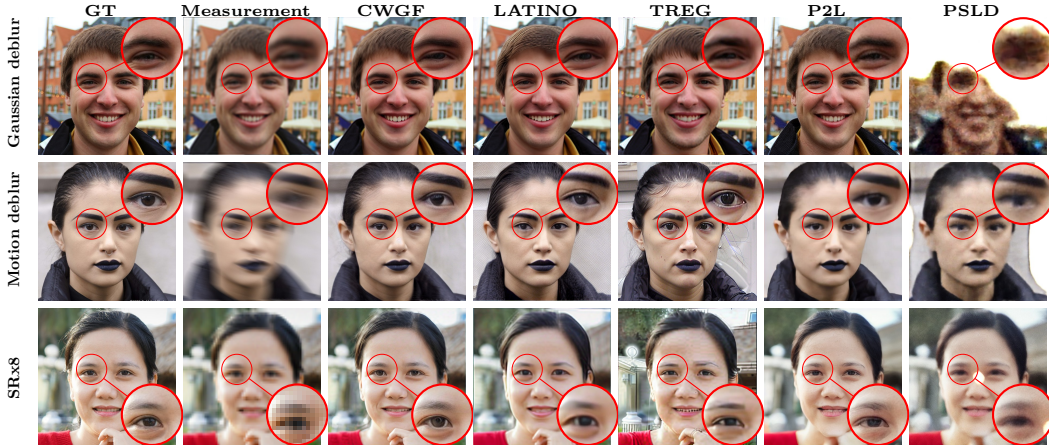


Figure 4: Qualitative comparison of image restoration results. Samples taken from FFHQ-512. Prompt: A photo of a face.

Drifting a wrong prompt. To verify that our joint posterior-prompt optimisation is effective, we conduct experiments on the FFHQ test dataset, in which the initial prompt is misinitialised as **A photo of a cat**. We compare the method’s results when prompt optimisation is disabled (CWGF (no prompt opt.) row in Table 2) with those of the full CWGF algorithm. We also compare our method with LATINO, LATINO-PRO, P2L, and TReg, showing improved semantic alignment. Indeed, while other methods fail to yield correct high-resolution features, CWGF improves prompt retrieval, which is necessary to correctly leverage the prior’s capabilities to generate such details.

Method	Gaussian				Motion			SR $\times 8$		
	NFE	FID	PSNR	LPIPS	FID	PSNR	LPIPS	FID	PSNR	LPIPS
CWGF (no prompt opt.)	16	<u>32.91</u>	<u>28.64</u>	0.354	<u>32.20</u>	<u>27.86</u>	<u>0.357</u>	92.43	<u>26.24</u>	0.456
LATINO-PRO	65	44.67	28.63	<u>0.331</u>	44.40	25.31	0.422	85.58	26.17	<u>0.452</u>
P2L	400	46.40	26.06	0.476	65.22	23.79	0.542	<u>80.68</u>	23.43	0.540
TReg	200	95.96	22.89	0.463	164.4	20.87	0.518	137.0	21.29	0.528
CWGF	16	27.58	29.59	0.322	25.99	28.16	0.339	50.07	27.39	0.415

Table 2: Negative prompt scenario on FFHQ-512 with prompt **A photo of a cat**. Results are reported for Gaussian deblurring, motion deblurring, and $\times 8$ super-resolution with $\sigma_y = 0.01$. **Bold**: best; underline: second best.

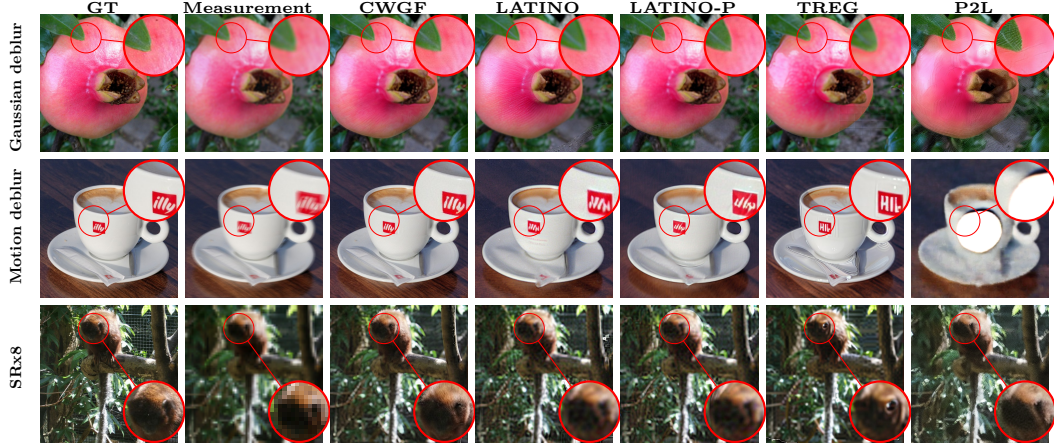


Figure 5: Qualitative comparison of image restoration results. Samples taken from ImageNet-512. Prompt: a photo in high resolution.



Figure 6: Qualitative comparison of image restoration results. Samples taken from FFHQ-512. Prompt: A photo of a cat.

5 Conclusion

We propose CWGF, a novel method for solving inverse problems with pre-trained text-to-image LCM priors. CWGF leverages a joint Euclidean-Wasserstein gradient flow over prompt embeddings and latent distributions. Extensive experiments show that CWGF delivers state-of-the-art performance with a significantly reduced computational cost. However, there remain some limitations that future work should address. First, while we have assumed a Euclidean geometry for the prompt embeddings, their geometry is not fully understood and future work should explore non-Euclidean constructions [Karris et al., 2025, Levi and Gilboa, 2025]. Second, CWGF is based on a consistency model prior, leaving extensions to other few-step models as future work [Boffi et al., 2025a,b, Geng et al., 2025, Deng et al., 2026].

Acknowledgments and Disclosure of Funding

MP acknowledges support by UKRI Engineering and Physical Sciences Research Council (EPSRC) (EP/V006134/1, EP/Z534481/1). AS acknowledges support from the France 2030 research program on artificial intelligence via the PEPR PDE-AI grant (ANR-23-PEIA-

0004). HPC resources provided by GENCI-IDRIS Jean-Zay (Grant 2024-AD011014557). TW is supported by the Roth Scholarship from the Department of Mathematics, Imperial College London. The authors acknowledge computational resources and support provided by the Department of Mathematics and the Imperial College Research Computing Service, DOI: 10.14469/hpc/2232. The authors acknowledge the use of resources provided by the Isambard-AI National AI Research Resource (AIRR) [McIntosh-Smith et al., 2024]. Isambard-AI is operated by the University of Bristol and is funded by the UK Governments Department for Science, Innovation and Technology (DSIT) via UK Research and Innovation; and the Science and Technology Facilities Council [ST/AIRR/I-A-I/1023].

References

- Idan Achituve, Hai Victor Habi, Amir Rosenfeld, Arnon Netzer, Idit Diamant, and Ethan Fetaya. Inverse problem sampling in latent space using sequential monte carlo, February 2025.
- O Deniz Akyildiz, Michela Ottobre, and Iain Souttar. A multiscale perspective on maximum marginal likelihood estimation. *arXiv preprint arXiv:2406.04187*, 2024.
- Luigi Ambrosio, Nicola Gigli, and Giuseppe Savare. *Gradient Flows: In Metric Spaces and in the Space of Probability Measures*. Springer Science & Business Media, 2008.
- Espen Bernton. Langevin Monte Carlo and JKO splitting. In Sébastien Bubeck, Vianney Perchet, and Philippe Rigollet, editors, *Proceedings of the 31st Conference On Learning Theory*, volume 75 of *Proceedings of Machine Learning Research*, pages 1777–1798. PMLR, 06–09 Jul 2018.
- Freddie Bickford Smith, Adam Foster, and Tom Rainforth. Making better use of unlabelled data in Bayesian active learning. *International Conference on Artificial Intelligence and Statistics*, 2024.
- Pier Giovanni Bissiri, Chris C Holmes, and Stephen G Walker. A general framework for updating belief distributions. *Journal of the Royal Statistical Society Series B: Statistical Methodology*, 78(5):1103–1130, 2016.
- Andreas Blattmann, Tim Dockhorn, Sumith Kulal, Daniel Mendelevitch, Maciej Kilian, Dominik Lorenz, Yam Levi, Zion English, Vikram Voleti, Adam Letts, et al. Stable video diffusion: Scaling latent video diffusion models to large datasets. *arXiv preprint arXiv:2311.15127*, 2023.
- Nicholas M. Boffi, Michael S. Albergo, and Eric Vanden-Eijnden. How to build a consistency model: Learning flow maps via self-distillation, 2025a.
- Nicholas M. Boffi, Michael S. Albergo, and Eric Vanden-Eijnden. Flow map matching with stochastic interpolants: A mathematical framework for consistency models, 2025b.
- Valentin De Bortoli, Alain Durmus, Marcelo Pereyra, and Ana F. Vidal. Efficient stochastic optimisation by unadjusted langevin monte carlo. application to maximum marginal likelihood and empirical bayesian estimation, 2020.
- Stephen P. Boyd, Neal Parikh, Eric Chu, Borja Peleato, and Jonathan Eckstein. Distributed optimization and statistical learning via the alternating direction method of multipliers. *Found. Trends Mach. Learn.*, 3:1–122, 2011.
- B. Boys, M. Girolami, J. Pidstrigach, S. Reich, A. Mosca, and O. D. Akyildiz. Tweedie moment projected diffusions for inverse problems. *Transactions on Machine Learning Research*, 2024. Featured Certification; ICLR 2025 Journal Track.
- Rocco Caprio, Juan Kuntz, Samuel Power, and Adam M. Johansen. Error bounds for particle gradient descent, and extensions of the log-sobolev and talagrand inequalities. *Journal of Machine Learning Research*, 26(103):1–38, 2025.

- Jaemoo Choi, Yuchen Zhu, Wei Guo, Petr Molodyk, Bo Yuan, Jinbin Bai, Yi Xin, Molei Tao, and Yongxin Chen. Rethinking the design space of reinforcement learning for diffusion models: On the importance of likelihood estimation beyond loss design, February 2026.
- Hyungjin Chung, Jeongsol Kim, Michael Thompson Mccann, Marc Louis Klasky, and Jong Chul Ye. Diffusion posterior sampling for general noisy inverse problems. In *The Eleventh International Conference on Learning Representations*, 2023.
- Hyungjin Chung, Jong Chul Ye, Peyman Milanfar, and Mauricio Delbracio. Prompt-tuning latent diffusion models for inverse problems. In *Forty-first International Conference on Machine Learning*, 2024.
- Philippe Clément and Jan Maas. A trotter product formula for gradient flows in metric spaces. *Journal of Evolution Equations*, 11(2):405–427, 2011.
- Arthur P Dempster, Nan M Laird, and Donald B Rubin. Maximum likelihood from incomplete data via the EM algorithm. *Journal of the royal statistical society: series B (methodological)*, 39(1):1–22, 1977.
- Jia Deng, Wei Dong, Richard Socher, Li-Jia Li, K. Li, and Li Fei-Fei. Imagenet: A large-scale hierarchical image database. *2009 IEEE Conference on Computer Vision and Pattern Recognition*, pages 248–255, 2009.
- Li Deng. The mnist database of handwritten digit images for machine learning research [best of the web]. *IEEE Signal Processing Magazine*, 29:141–142, 2012.
- Mingyang Deng, He Li, Tianhong Li, Yilun Du, and Kaiming He. Generative Modeling via Drifting, February 2026.
- Yann Dubois, Alexandros Kastanos, Dave Lines, and Bart Melman. Disentangling VAE, 2019.
- Alessio Figalli and Federico Glaudo. *An invitation to optimal transport, Wasserstein distances, and gradient flows*. EMS textbooks in mathematics. European Mathematical Society, 2021. ISBN 9783985475100.
- Rinon Gal, Yuval Alaluf, Yuval Atzmon, Or Patashnik, Amit H. Bermano, Gal Chechik, and Daniel Cohen-Or. An image is worth one word: Personalizing text-to-image generation using textual inversion, 2022.
- Tomer Garber and Tom Tirer. Zero-shot image restoration using few-step guidance of consistency models (and beyond). In *Proceedings of the Computer Vision and Pattern Recognition Conference (CVPR)*, pages 2398–2407, June 2025.
- Richard Gardner. The brunn-minkowski inequality. *Bulletin of the American mathematical society*, 39(3):355–405, 2002.
- Zhengyang Geng, Mingyang Deng, Xingjian Bai, J. Zico Kolter, and Kaiming He. Mean flows for one-step generative modeling. *arXiv preprint arXiv:2505.13447*, 2025.
- Sai Bharath Chandra Gutha, Ricardo Vinuesa, and Hossein Azizpour. Mode-seeking for inverse problems with diffusion models, December 2025.
- Jonathan Ho, Ajay Jain, and Pieter Abbeel. Denoising diffusion probabilistic models. *Advances in neural information processing systems*, 33:6840–6851, 2020.
- Jonathan Ho, William Chan, Chitwan Saharia, Jay Whang, Ruiqi Gao, Alexey Gritsenko, Diederik P. Kingma, Ben Poole, Mohammad Norouzi, David J. Fleet, and Tim Salimans. Imagen video: High definition video generation with diffusion models, 2022.
- Edward J Hu, yelong shen, Phillip Wallis, Zeyuan Allen-Zhu, Yuanzhi Li, Shean Wang, Lu Wang, and Weizhu Chen. LoRA: Low-rank adaptation of large language models. In *International Conference on Learning Representations*, 2022.

- Yazid Janati, Badr Moufad, Alain Durmus, Eric Moulines, and Jimmy Olsson. Divide-and-conquer posterior sampling for denoising diffusion priors. *Advances in Neural Information Processing Systems*, 37:97408–97444, 2024.
- Tero Karras, Samuli Laine, and Timo Aila. A style-based generator architecture for generative adversarial networks. In *2019 IEEE/CVF Conference on Computer Vision and Pattern Recognition (CVPR)*, pages 4396–4405, 2019.
- Tero Karras, Miika Aittala, Timo Aila, and Samuli Laine. Elucidating the Design Space of Diffusion-Based Generative Models. *Neural Information Processing Systems*, abs/2206.00364, June 2022. doi: 10.48550/arXiv.2206.00364.
- Nicholas Karris, Luke Durell, Javier Flores, and Tegan Emerson. Which Way from B to A: The role of embedding geometry in image interpolation for Stable Diffusion, November 2025.
- Bahjat Kawar, Michael Elad, Stefano Ermon, and Jiaming Song. Denoising diffusion restoration models. *Advances in Neural Information Processing Systems*, 35:23593–23606, 2022.
- Dongjun Kim, Chieh-Hsin Lai, Wei-Hsiang Liao, Naoki Murata, Yuhta Takida, Toshimitsu Uesaka, Yutong He, Yuki Mitsufuji, and Stefano Ermon. Consistency trajectory models: Learning probability flow ode trajectory of diffusion. *arXiv preprint arXiv:2310.02279*, 2023.
- Jeongsol Kim, Geon Yeong Park, Hyungjin Chung, and Jong Chul Ye. Regularization by texts for latent diffusion inverse solvers, 2025a.
- Kunhee Kim, NaHyeon Park, Kibeom Hong, and Hyunjung Shim. Directional textual inversion for personalized text-to-image generation, December 2025b.
- Taehoon Kim, Henry Gouk, and Timothy Hospedales. Test-time alignment of text-to-image diffusion models via null-text embedding optimisation, 2025c.
- Diederik P. Kingma and Jimmy Ba. Adam: A method for stochastic optimization. *International Conference on Learning Representations*, 2014.
- Diederik P. Kingma and Ruiqi Gao. Understanding Diffusion Objectives as the ELBO with Simple Data Augmentation. *Neural Information Processing Systems*, March 2023. doi: 10.48550/arXiv.2303.00848.
- Diederik P. Kingma and Max Welling. Auto-encoding variational bayes. *CoRR*, abs/1312.6114, 2013.
- Juan Kuntz, Jen Ning Lim, and Adam M. Johansen. Particle algorithms for maximum likelihood training of latent variable models. In *Proceedings of The 26th International Conference on Artificial Intelligence and Statistics*, volume 206 of *Proceedings of Machine Learning Research*, 2023.
- Taesung Kwon and Jong Chul Ye. Vision-xl: High definition video inverse problem solver using latent image diffusion models, 2025.
- Taesung Kwon, Gookho Song, Yoosun Kim, Jeongsol Kim, Jong Chul Ye, and Mooseok Jang. Video diffusion posterior sampling for seeing beyond dynamic scattering layers. *IEEE transactions on pattern analysis and machine intelligence*, PP, 2025.
- Gustav Larsson, Michael Maire, and Gregory Shakhnarovich. Learning representations for automatic colorization. *ArXiv*, abs/1603.06668, 2016.
- Meir Yossef Levi and Guy Gilboa. The Double-Ellipsoid Geometry of CLIP, May 2025.
- Xiang Li, Soo Min Kwon, Shijun Liang, Ismail R. Alkhouri, Saiprasad Ravishankar, and Qing Qu. Decoupled data consistency with diffusion purification for image restoration, 2025.

- Romain Lopez, Pierre Boyeau, Nir Yosef, Michael I. Jordan, and Jeffrey Regier. Auto-encoding variational bayes. In *Proceedings of the Neural Information Processing Systems Conference*, 2020.
- Cheng Lu and Yang Song. Simplifying, stabilizing and scaling continuous-time consistency models, 2025.
- Eric Luhman and Troy Luhman. Knowledge distillation in iterative generative models for improved sampling speed. *ArXiv*, abs/2101.02388, 2021.
- Simian Luo, Yiqin Tan, Longbo Huang, Jian Li, and Hang Zhao. Latent consistency models: Synthesizing high-resolution images with few-step inference. *ArXiv*, abs/2310.04378, 2023a.
- Simian Luo, Yiqin Tan, Suraj Patil, Daniel Gu, Patrick von Platen, Apolinário Passos, Longbo Huang, Jian Li, and Hang Zhao. Lcm-lora: A universal stable-diffusion acceleration module, 2023b.
- Weijian Luo, Tianyang Hu, Shifeng Zhang, Jiacheng Sun, Zhenguo Li, and Zhihua Zhang. Diff-instruct: A universal approach for transferring knowledge from pre-trained diffusion models. *ArXiv*, abs/2305.18455, 2023c.
- Shweta Mahajan, Tanzila Rahman, Kwang Moo Yi, and Leonid Sigal. Prompting hard or hardly prompting: Prompt inversion for text-to-image diffusion models. In *2024 IEEE/CVF Conference on Computer Vision and Pattern Recognition (CVPR)*, pages 6808–6817, Seattle, WA, USA, June 2024. IEEE. ISBN 979-8-3503-5300-6. doi: 10.1109/CVPR52733.2024.00650.
- Morteza Mardani, Jiaming Song, Jan Kautz, and Arash Vahdat. A variational perspective on solving inverse problems with diffusion models. In *The Twelfth International Conference on Learning Representations*, 2024.
- Charlesquin Kemajou Mbakam, Jonathan Spence, and Marcelo Pereyra. Learning few-step posterior samplers by unfolding and distillation of diffusion models. *Trans. Mach. Learn. Res.*, 2025, 2025.
- Simon McIntosh-Smith, Sadaf R Alam, and Christopher Woods. Isambard-ai: a leadership class supercomputer optimised specifically for artificial intelligence, 2024. URL <https://arxiv.org/abs/2410.11199>.
- Ron Mokady, Amir Hertz, Kfir Aberman, Yael Pritch, and Daniel Cohen-Or. Null-text inversion for editing real images using guided diffusion models, 2022.
- Badr Moufad, Yazid Janati, Lisa Bedin, Alain Oliviero Durmus, randal douc, Eric Moulines, and Jimmy Olsson. Variational diffusion posterior sampling with midpoint guidance. In *The Thirteenth International Conference on Learning Representations*, 2025.
- Felix Otto. The geometry of dissipative evolution equations: The porous medium equation. *Communications in Partial Differential Equations*, 26(1-2):101–174, 2001.
- Grigorios A. Pavliotis and Andrew M. Stuart. *Averaging for ODEs and SDEs*, pages 145–156. Springer New York, New York, NY, 2008.
- Dustin Podell, Zion English, Kyle Lacey, Andreas Blattmann, Tim Dockhorn, Jonas Müller, Joe Penna, and Robin Rombach. Sd-xl: Improving latent diffusion models for high-resolution image synthesis. In *The Twelfth International Conference on Learning Representations*, 2023.
- Alec Radford, Jong Wook Kim, Chris Hallacy, Aditya Ramesh, Gabriel Goh, Sandhini Agarwal, Girish Sastry, Amanda Askell, Pamela Mishkin, Jack Clark, Gretchen Krueger, and Ilya Sutskever. Learning transferable visual models from natural language supervision. In *International Conference on Machine Learning*, 2021.

- Ron Raphaeli, Sean Man, and Michael Elad. SILO: Solving inverse problems with latent operators, January 2025.
- Robin Rombach, A. Blattmann, Dominik Lorenz, Patrick Esser, and Björn Ommer. High-resolution image synthesis with latent diffusion models. *2022 IEEE/CVF Conference on Computer Vision and Pattern Recognition (CVPR)*, pages 10674–10685, 2021.
- Robin Rombach, Andreas Blattmann, Dominik Lorenz, Patrick Esser, and Björn Ommer. High-resolution image synthesis with latent diffusion models. In *Proceedings of the IEEE/CVF Conference on Computer Vision and Pattern Recognition (CVPR)*, 2022.
- Litu Rout, Negin Raoof, Giannis Daras, Constantine Caramanis, Alex Dimakis, and Sanjay Shakkottai. Solving linear inverse problems provably via posterior sampling with latent diffusion models. In *Thirty-seventh Conference on Neural Information Processing Systems*, 2023.
- Tim Salimans, Thomas Mensink, Jonathan Heek, and Emiel Hoogeboom. Multistep distillation of diffusion models via moment matching. *ArXiv*, abs/2406.04103, 2024.
- Filippo Santambrogio. *Optimal transport for applied mathematicians*. Springer, 2015.
- Filippo Santambrogio. Euclidean, Metric, and Wasserstein gradient flows: an overview. *arXiv preprint arXiv:1609.03890*, 2016.
- Axel Sauer, Dominik Lorenz, A. Blattmann, and Robin Rombach. Adversarial diffusion distillation. In *European Conference on Computer Vision*, 2023.
- Abduragim Shtanchaev, Albina Ilina, Yazid Janati, Arip Asadulaev, Martin Takác, and Eric Moulines. Guess & guide: Gradient-free zero-shot diffusion guidance, March 2026.
- Marta Skreta, Lazar Atanackovic, Joey Bose, Alexander Tong, and Kirill Neklyudov. The superposition of diffusion models using the itô density estimator. In *The Thirteenth International Conference on Learning Representations*, 2025.
- Jascha Narain Sohl-Dickstein, Eric A. Weiss, Niru Maheswaranathan, and Surya Ganguli. Deep unsupervised learning using nonequilibrium thermodynamics. *ArXiv*, abs/1503.03585, 2015.
- Bowen Song, Soo Min Kwon, Zecheng Zhang, Xinyu Hu, Qing Qu, and Liyue Shen. Solving inverse problems with latent diffusion models via hard data consistency. In *The Twelfth International Conference on Learning Representations*, 2024.
- Jiaming Song, Chenlin Meng, and Stefano Ermon. Denoising diffusion implicit models. *ArXiv*, abs/2010.02502, 2020a.
- Jiaming Song, Arash Vahdat, Morteza Mardani, and Jan Kautz. Pseudoinverse-guided diffusion models for inverse problems. In *International Conference on Learning Representations*, 2023a.
- Yang Song and Prafulla Dhariwal. Improved techniques for training consistency models, 2023.
- Yang Song and Stefano Ermon. Generative modeling by estimating gradients of the data distribution. In *Neural Information Processing Systems*, 2019.
- Yang Song and Stefano Ermon. Improved techniques for training score-based generative models. *Advances in neural information processing systems*, 33:12438–12448, 2020.
- Yang Song, Jascha Sohl-Dickstein, Diederik P Kingma, Abhishek Kumar, Stefano Ermon, and Ben Poole. Score-based generative modeling through stochastic differential equations. In *International Conference on Learning Representations*, 2020b.
- Yang Song, Conor Durkan, Iain Murray, and Stefano Ermon. Maximum likelihood training of score-based diffusion models. *Neural Information Processing Systems*, pages 1415–1428, January 2021a. doi: 10.48550/arXiv.2101.09258.

- Yang Song, Jascha Sohl-Dickstein, Diederik P Kingma, Abhishek Kumar, Stefano Ermon, and Ben Poole. Score-based generative modeling through stochastic differential equations. In *International Conference on Learning Representations*, 2021b.
- Yang Song, Prafulla Dhariwal, Mark Chen, and I. Sutskever. Consistency models. *International Conference on Machine Learning*, 2023b.
- Alessio Spagnoletti, Andr'es Almansa, and Marcelo Pereyra. Lvtino: Latent video consistency inverse solver for high definition video restoration. *ArXiv*, abs/2510.01339, 2025a.
- Alessio Spagnoletti, Jean Prost, Andr'es Almansa, Nicolas Papadakis, and Marcelo Pereyra. Latino-pro: Latent consistency inverse solver with prompt optimization. In *Proceedings of the IEEE/CVF International Conference on Computer Vision (ICCV)*, pages 19597–19607, October 2025b.
- Andrew M Stuart. Inverse problems: a bayesian perspective. *Acta numerica*, 19:451–559, 2010.
- Cédric Villani. *Topics in optimal transportation*. Graduate studies in mathematics ; v. 58. American Mathematical Society, 2003.
- Pascal Vincent. A connection between score matching and denoising autoencoders. *Neural Computation*, 23:1661–1674, 2011.
- Team Wan, Ang Wang, Baole Ai, Bin Wen, Chaojie Mao, Chen-Wei Xie, Di Chen, Feiwu Yu, Haiming Zhao, Jianxiao Yang, Jianyuan Zeng, Jiayu Wang, Jingfeng Zhang, Jingren Zhou, Jinkai Wang, Jixuan Chen, Kai Zhu, Kang Zhao, Keyu Yan, Lianghua Huang, Mengyang Feng, Ningyi Zhang, Pandeng Li, Pingyu Wu, Ruihang Chu, Ruili Feng, Shiwei Zhang, Siyang Sun, Tao Fang, Tianxing Wang, Tianyi Gui, Tingyu Weng, Tong Shen, Wei Lin, Wei Wang, Wei Wang, Wenmeng Zhou, Wenten Wang, Wenting Shen, Wenyuan Yu, Xianzhong Shi, Xiaoming Huang, Xin Xu, Yan Kou, Yangyu Lv, Yifei Li, Yijing Liu, Yiming Wang, Yingya Zhang, Yitong Huang, Yong Li, You Wu, Yu Liu, Yulin Pan, Yun Zheng, Yuntao Hong, Yupeng Shi, Yutong Feng, Zeyinzi Jiang, Zhen Han, Zhi-Fan Wu, and Ziyu Liu. Wan: Open and advanced large-scale video generative models. *arXiv preprint arXiv:2503.20314*, 2025.
- He Wang, Longquan Dai, and Jinhui Tang. EMControl: Adding conditional control to text-to-image diffusion models via expectation-maximization. *Proceedings of the AAAI Conference on Artificial Intelligence*, 39(7):7691–7699, April 2025a. doi: 10.1609/aaai.v39i7.32828.
- Ruochen Wang, Ting Liu, Cho-Jui Hsieh, and Boqing Gong. On discrete prompt optimization for diffusion models, June 2024.
- Tim Y. J. Wang and O. Deniz Akyildiz. A gradient flow approach to solving inverse problems with latent diffusion models, 2025.
- Yifei Wang, Weimin Bai, Colin Zhang, Debing Zhang, Weijian Luo, and He Sun. Uni-instruct: One-step diffusion model through unified diffusion divergence instruction, October 2025b.
- Zhendong Wang, Huangjie Zheng, Pengcheng He, Weizhu Chen, and Mingyuan Zhou. Diffusion-gan: Training gans with diffusion. *ArXiv*, abs/2206.02262, 2022.
- Zhengyi Wang, Cheng Lu, Yikai Wang, Fan Bao, Chongxuan Li, Hang Su, and Jun Zhu. Prolificdreamer: High-fidelity and diverse text-to-3d generation with variational score distillation. In *Thirty-seventh Conference on Neural Information Processing Systems*, 2023.
- Yuxin Wen, Neel Jain, John Kirchenbauer, Micah Goldblum, Jonas Geiping, and Tom Goldstein. Hard prompts made easy: Gradient-based discrete optimization for prompt tuning and discovery. In *Thirty-Seventh Conference on Neural Information Processing Systems*, November 2023.

- Andre Wibisono. Sampling as optimization in the space of measures: The langevin dynamics as a composite optimization problem. In Sébastien Bubeck, Vianney Perchet, and Philippe Rigollet, editors, *Proceedings of the 31st Conference On Learning Theory*, volume 75 of *Proceedings of Machine Learning Research*, pages 2093–3027. PMLR, 06–09 Jul 2018.
- Tongda Xu, Ziran Zhu, Jian Li, Dailan He, Yuanyuan Wang, Ming Sun, Ling Li, Hongwei Qin, Yan Wang, Jingjing Liu, and Ya-Qin Zhang. Consistency model is an effective posterior sample approximation for diffusion inverse solvers, 2024.
- Tianwei Yin, Michaël Gharbi, Richard Zhang, Eli Shechtman, Frédo Durand, William T Freeman, and Taesung Park. One-step diffusion with distribution matching distillation. In *2024 IEEE/CVF Conference on Computer Vision and Pattern Recognition (CVPR)*, 2024a.
- Tianwei Yin, Michaël Gharbi, Taesung Park, Richard Zhang, Eli Shechtman, Fredo Durand, and William T. Freeman. Improved distribution matching distillation for fast image synthesis. *arXiv preprint arXiv:2405.14867*, 2024b.
- Jiankun Zhao, Bowen Song, and Liyue Shen. Cosign: Few-step guidance of consistency model to solve general inverse problems. In *European Conference on Computer Vision*, pages 108–126. Springer, 2024.
- Hongkai Zheng, Weili Nie, Arash Vahdat, Kamyar Aizzadenesheli, and Anima Anandkumar. Fast sampling of diffusion models via operator learning. In *International Conference on Machine Learning*, 2022.
- Léon Zheng, Thomas Hirtz, Yazid Janati, and Eric Moulines. Fast and Robust Likelihood-Guided Diffusion Posterior Sampling with Amortized Variational Inference, February 2026.
- Yuanzhi Zhu, Kai Zhang, Jingyun Liang, Jiezhong Cao, Bihan Wen, Radu Timofte, and Luc Van Gool. Denoising Diffusion Models for Plug-and-Play Image Restoration. In *2023 IEEE/CVF Conference on Computer Vision and Pattern Recognition Workshops (CVPRW)*, May 2023. doi: 10.1109/CVPRW59228.2023.00129.
- Nicolas Zilberstein, Morteza Mardani, and Santiago Segarra. Repulsive latent score distillation for solving inverse problems. In *The Thirteenth International Conference on Learning Representations*, 2025.

A Derivations and Proofs

A.1 Background on $\mathbb{C} \times \mathcal{P}_2(\mathbb{Z})$'s Geometry

Geometric Constructions. We endow the product space $\mathbb{C} \times \mathcal{P}_2(\mathbb{Z})$ with geometry induced by the Wasserstein-2 metric on $\mathcal{P}_2(\mathbb{Z})$ and the Euclidean metric on \mathbb{C} similarly to Kuntz et al. [2023]. The tangent space at a point (\mathbf{c}, μ) is given by:

$$T_{(\mathbf{c}, \mu)}(\mathbb{C} \times \mathcal{P}_2(\mathbb{Z})) = T_{\mathbf{c}}(\mathbb{C}) \times T_{\mu}(\mathcal{P}_2(\mathbb{Z})), \quad (26)$$

where $T_{\mathbf{c}}(\mathbb{C})$ is the usual Euclidean space and $T_{\mu}(\mathcal{P}_2(\mathbb{Z}))$ is the tangent space at μ defined by the Wasserstein-2 geometry [Otto, 2001, Figalli and Glaudo, 2021]:

$$T_{\mu}(\mathcal{P}_2(\mathbb{Z})) = \{\partial_t \mu_t|_{t=0} \mid \partial_t \mu_t + \nabla \cdot (\mu_t v_t) = 0, \mu_0 = \mu, v_t = \nabla \psi_t, \psi_t \in C_c^\infty(\mathbb{Z})\}. \quad (27)$$

We define the Riemannian metric on the tangent space as a product metric:

$$\langle (u_1, v_1), (u_2, v_2) \rangle_{(\mathbf{c}, \mu)} = \langle u_1, u_2 \rangle + \langle v_1, v_2 \rangle_{\mu}, \quad (28)$$

where $\langle u_1, u_2 \rangle$ is the standard Euclidean inner product and $\langle v_1, v_2 \rangle_{\mu}$ is the Wasserstein-2 inner product defined as:

$$\langle v_1, v_2 \rangle_{\mu} = \int \nabla \psi_{v_1}(\mathbf{z}) \cdot \nabla \psi_{v_2}(\mathbf{z}) \mu(\mathbf{z}) d\mathbf{z}, \quad (29)$$

where ψ_{v_1} and ψ_{v_2} are the potentials associated with the vector fields v_1 and v_2 satisfying $v_i = -\nabla \cdot (\mu \nabla \psi_{v_i})$ for $i = 1, 2$. In what follows, we restrict to the subspace of distributions that have probability densities w.r.t. the Lebesgue measure and we thus use $\mathcal{P}_2(\mathbb{Z})$ interchangeably with $\mathcal{P}_{2,a.c.}(\mathbb{Z})$.

The Gradient. The Wasserstein-2 gradient at $\mu \in \mathcal{P}_2(\mathbb{Z})$ is the unique tangent vector in $\text{grad}_{W_2} \mathcal{L}[\mu] \in T_{\mu} \mathcal{P}_2(\mathbb{Z})$ such that for any tangent vector $v \in T_{\mu} \mathcal{P}_2(\mathbb{Z})$, we have:

$$\langle \text{grad}_{W_2} \mathcal{L}[\mu], v \rangle_{\mu} = \lim_{\varepsilon \rightarrow 0} \frac{\mathcal{L}[\mu_{\varepsilon}] - \mathcal{L}[\mu]}{\varepsilon}, \quad (30)$$

for any smooth curve $\mu_{\varepsilon} : (-\varepsilon_0, \varepsilon_0) \rightarrow \mathcal{P}_2(\mathbb{Z})$ satisfying $\mu_0 = \mu$ and $\partial_{\varepsilon} \mu_{\varepsilon}|_{\varepsilon=0} = v$.

For a regular functional $\mathcal{L} : \mathcal{P}_2(\mathbb{Z}) \rightarrow \mathbb{R}$ satisfying the assumptions discussed in Ambrosio et al. [2008, 10.4.1], we define its first variation at μ as the unique function $\delta \mathcal{L} / \delta \mu : \mathbb{Z} \rightarrow \mathbb{R}$ satisfying:

$$\lim_{\varepsilon \searrow 0} \frac{\mathcal{L}[\mu + \varepsilon \chi] - \mathcal{L}[\mu]}{\varepsilon} = \int \frac{\delta \mathcal{L}}{\delta \mu}(\mathbf{z}) \chi(d\mathbf{z}), \quad (31)$$

for all signed measures χ such that $\mu + \varepsilon \chi \in \mathcal{P}_2(\mathbb{Z})$ for all sufficiently small ε . The Wasserstein-2 gradient of \mathcal{L} at μ is given by [Figalli and Glaudo, 2021, Chapter 4]:

$$\text{grad}_{W_2} \mathcal{L}[\mu] = -\nabla \cdot \left(\mu \nabla \frac{\delta \mathcal{L}}{\delta \mu} \right). \quad (32)$$

Therefore, for a functional $\mathcal{F} : \mathbb{C} \times \mathcal{P}_2(\mathbb{Z}) \rightarrow \mathbb{R}$ defined on the product manifold that is differentiable in c and regular in μ , the gradient at (c, μ) is given by:

$$\nabla \mathcal{F}[c, \mu] := \left(\nabla_c \mathcal{F}[c, \mu], \text{grad}_{W_2} \mathcal{F}[c, \mu] \right). \quad (33)$$

We first state a standard result on the first variation of the KL divergence. (cf. Villani [2003], Santambrogio [2016], Figalli and Glaudo [2021])

Lemma 1 (First Variation of KL Divergence). *For $p, q \in \mathcal{P}_2(\mathbb{Z})$, the first variation of the KL divergence is given by:*

$$\frac{\delta D_{\text{KL}}(q||p)}{\delta q}(z) = \log q(z) - \log p(z) + 1, \quad \forall z \in \mathbb{Z} \quad (34)$$

Proof. Using the equivalent definition of first variation, we can write for $m \in T\mathcal{P}_2(\mathbf{Z})$ and $t > 0$:

$$D_{\text{KL}}(q + tm||p) = D_{\text{KL}}(q||p) + t \left\langle m, \frac{\delta D_{\text{KL}}(q||p)}{\delta q} \right\rangle + o(t), \quad (35)$$

where the inner product is defined $\langle m, f \rangle := \int_{\mathbf{Z}} f(z)m(z)dz$ for all $f, m \in T\mathcal{P}_2(\mathbf{Z})$. Using Taylor expansion of $(z+t)\log(z+t) = z\log z + t(\log z + 1) + o(t)$, we can write $D_{\text{KL}}(q + tm||p)$ as:

$$D_{\text{KL}}(q + tm||p) = \int (q(z) + tm(z))[\log(q(z) + tm(z)) - \log p(z)]dz \quad (36)$$

$$= \int q(z)\log q(z)dz - \int q(z)\log p(z)dz \quad (37)$$

$$+ t \int (\log q(z) - \log p(z) + 1)m(z)dz + o(t), \quad (38)$$

which shows the desired result by matching the terms. \square

As a consequence, the Wasserstein-2 gradient of the KL divergence is given by:

$$\text{grad}_{W_2} D_{\text{KL}}(q||p) = -\nabla \cdot \left(q \nabla \log \frac{q}{p} \right). \quad (39)$$

Lemma 2. For $\mathcal{L} : \mathcal{P}_2(\mathbf{Z}) \rightarrow \mathbb{R}$ with $\mathcal{L}[\mu] := \int w(z)\mu(z)dz$ for any fixed $w(z) : \mathbb{R}^d \rightarrow \mathbb{R}$, we have:

$$\frac{\delta \mathcal{L}[\mu]}{\delta \mu}(z) = w(z) \quad (40)$$

Proof. Similar to the proof above, for any $m \in T\mathcal{P}_2(\mathbf{Z})$ and $t \in \mathbb{R}$, we have:

$$\mathcal{L}[\mu + tm] = \int w(z)(\mu(z) + tm(z))dz \quad (41)$$

$$= \int w(z)\mu(z)dz + t \int w(z)m(z)dz. \quad (42)$$

From the definition of the functional derivative, this implies the desired result. \square

A.2 Proof to Theorem 1

Proof. By the definition of grad_{W_2} , $\text{grad}_{W_2} \mathcal{F}[c, \mu] = 0$ if and only if $\mu = p_c(\mathbf{z}|\mathbf{y})$, which is the optimal solution to $\arg \min D_{\text{KL}}(\mu||p_c) - \mathbb{E}_\mu[\log p(\mathbf{y}|\mathbf{z})]$. Moreover, we have from $p_c(\mathbf{y}, \mathbf{z}) = p(\mathbf{y}|\mathbf{z})p_c(\mathbf{z})$ that

$$\begin{aligned} \nabla_c p_c(\mathbf{y}) &= \int \nabla_c p_c(\mathbf{y}, \mathbf{z})d\mathbf{z} = \int \nabla_c \log p_c(\mathbf{z})p_c(\mathbf{z}|\mathbf{y})p_c(\mathbf{y})d\mathbf{z} \\ &= p_c(\mathbf{y})\nabla_c D_{\text{KL}}(\mu||p_c) \end{aligned}$$

Thus, $\nabla_c p_c(\mathbf{y}) = 0$ if and only if $\nabla_c \mathcal{R}[c, \mu] = \nabla_c D_{\text{KL}}(\mu||p_c) = 0$. The result follows by combining the two conditions. \square

A.3 Exponential Convergence to the Minimisers

To prove the exponential convergence, we first need two standard assumptions on the regularity of the model and the strong log-concavity of the likelihood and the prior.

Assumption 2 (Model Regularity). *i) For all $\mathbf{z} \in \mathbf{Z}$, the maps $c \mapsto \log p_c(\mathbf{z}|\mathbf{y})$ and $c \mapsto \log p_c(\mathbf{y})$ are differentiable; ii) for all $c \in \mathbf{C}$, $c \mapsto p_c(\mathbf{z}|\mathbf{y})$ is twice continuously differentiable; iii) for all $c \in \mathbf{C}$ and $\mathbf{z} \in \mathbf{Z}$, the joint density $p_c(\mathbf{y}, \mathbf{z})$ is positive everywhere.*

Assumption 3 (Strong Log-Concavity). *i) The map $(c, \mathbf{z}) \mapsto \log p_c(\mathbf{z})$ is jointly λ -strongly concave; ii) $p(\mathbf{y}|\mathbf{x})p_{\phi^-}(\mathbf{z}|\mathbf{y})$ is λ' -strongly log-concave.*

Remark 1. We note that in the case of a linear inverse problem, $p(\mathbf{y}|\mathbf{x})$ is Gaussian and thus log-concave. Moreover, if the decoder is linear Gaussian, then $p_\phi(\mathbf{z}|\mathbf{y})$ is also strongly log-concave.

Theorem 4 (Exponential convergence). *Under Assumptions 2 and 3, the functional $\mathcal{F}[c, \mu]$ has a unique minimiser (c_\star, μ_\star) and for $\tilde{\lambda} := \min(\lambda, \lambda')$ the flow in (10)-(11) converges exponentially fast to (c_\star, μ_\star)*

$$d_{W_2}(\mu_\tau, \mu_\star)^2 + \|c_\tau - c_\star\|_2^2 \leq 2\tilde{\lambda}^{-1}e^{-2\tilde{\lambda}\tau}(\mathcal{F}[c_0, \mu_0] - \mathcal{F}[c_\star, \mu_\star]). \quad (43)$$

Proof. The proof follows uses the same strategy as in Caprio et al. [2025]. Define $\ell(c, \mathbf{z}) := \log p_c(\mathbf{y}, \mathbf{z}) = \log \int p(\mathbf{y}|\mathbf{x})p(\mathbf{x}|\mathbf{z})p_c(\mathbf{z})d\mathbf{x}$. We first show that $\ell(c, \mathbf{z})$ is strongly concave in (c, \mathbf{z}) . Indeed, we have $\ell(c, \mathbf{z}) = \log p_c(\mathbf{z}) + \log \int p(\mathbf{y}|\mathbf{x})p(\mathbf{x}|\mathbf{z})d\mathbf{x}$, where the first term is λ -strongly concave by Assumption 3, and the second term is λ' -strongly concave in \mathbf{z} by the strong log-concavity of $p(\mathbf{y}|\mathbf{x})p(\mathbf{x}|\mathbf{z})$ and the Prékopa-Leindler inequality [Gardner, 2002, Theorem 7.1]. It follows that for any $t \in [0, 1]$ and $(c, \mathbf{z}), (c', \mathbf{z}') \in \mathbb{C} \times \mathbb{Z}$,

$$\begin{aligned} \ell((1-t)c + tc', (1-t)\mathbf{z} + t\mathbf{z}') &\geq (1-t)\ell(c, \mathbf{z}) + t\ell(c', \mathbf{z}') \\ &+ \frac{\lambda}{2}t(1-t)(\|c - c'\|_2^2 + \|\mathbf{z} - \mathbf{z}'\|_2^2) + \frac{\lambda'}{2}t(1-t)\|\mathbf{z} - \mathbf{z}'\|_2^2 \\ &\geq (1-t)\ell(c, \mathbf{z}) + t\ell(c', \mathbf{z}') + \frac{\min(\lambda, \lambda')}{2}t(1-t)(\|c - c'\|_2^2 + \|\mathbf{z} - \mathbf{z}'\|_2^2). \end{aligned}$$

Thus, under the log-concavity of $\ell(c, \mathbf{z})$ and Assumption 2, we can apply a similar argument to Kuntz et al. [2023, Theorem 4, Appendix B.3] to obtain the existence and uniqueness of the minimiser (c_\star, μ_\star) of $\log p_c(\mathbf{y})$. The result follows directly from Caprio et al. [2025, Corollary 5] given the log-concavity of $\ell(c, \mathbf{z})$ and the regularity of the model. \square

A.4 Proof to Proposition 1

Proof. Fix $r \in \mathcal{P}_2(\mathbb{Z})$ and let $r_s = Q_s \ast r$. Along the probability-flow characteristic associated with r_s , we have

$$\frac{dz_s^r}{ds} = -\frac{\beta_s}{2}z_s^r - \frac{\beta_s}{2}\nabla \log r_s(z_s^r), \quad s \in [0, t],$$

with terminal condition $z_t^r = z_t$ and initial point $z_0^r = G_t^r(z_t)$. Using $\frac{d}{ds}\alpha_s^{-1/2} = \frac{\beta_s}{2}\alpha_s^{-1/2}$, we obtain

$$\begin{aligned} \frac{d}{ds} \left(\frac{z_s^r}{\sqrt{\alpha_s}} \right) &= \frac{1}{\sqrt{\alpha_s}} \frac{dz_s^r}{ds} + \frac{\beta_s}{2\sqrt{\alpha_s}} z_s^r \\ &= -\frac{\beta_s}{2\sqrt{\alpha_s}} \nabla \log r_s(z_s^r). \end{aligned}$$

Integrating from 0 to t and using $\alpha_0 = 1$ gives

$$\frac{z_t}{\sqrt{\alpha_t}} - G_t^r(z_t) = -\int_0^t \frac{\beta_s}{2\sqrt{\alpha_s}} \nabla \log r_s(z_s^r) ds.$$

Equivalently,

$$G_t^r(z_t) = \frac{z_t}{\sqrt{\alpha_t}} + \int_0^t \frac{\beta_s}{2\sqrt{\alpha_s}} \nabla \log r_s(z_s^r) ds.$$

Multiplying by $\sqrt{\alpha_t}$, subtracting z_t , and dividing by $\sigma_t^2 = 1 - \alpha_t$ yields

$$\frac{\sqrt{\alpha_t}G_t^r(z_t) - z_t}{\sigma_t^2} = \frac{\sqrt{\alpha_t}}{\sigma_t^2} \int_0^t \frac{\beta_s}{2\sqrt{\alpha_s}} \nabla \log r_s(z_s^r) ds.$$

Multiplying both sides by $1 + \sqrt{\alpha_t}$ gives

$$(1 + \sqrt{\alpha_t}) \frac{\sqrt{\alpha_t}G_t^r(z_t) - z_t}{\sigma_t^2} = \int_0^t \gamma_t(s) \nabla \log r_s(z_s^r) ds,$$

where

$$\gamma_t(s) := \frac{(1 + \sqrt{\alpha_t})\sqrt{\alpha_t}}{\sigma_t^2} \frac{\beta_s}{2\sqrt{\alpha_s}} = \frac{\sqrt{\alpha_t}}{1 - \sqrt{\alpha_t}} \frac{\beta_s}{2\sqrt{\alpha_s}}$$

It remains to check that γ_t is a probability density on $[0, t]$. Since $\beta_s \geq 0$ and $\alpha_s > 0$, we have $\gamma_t(s) \geq 0$. Moreover,

$$\int_0^t \frac{\beta_s}{2\sqrt{\alpha_s}} ds = \frac{1}{\sqrt{\alpha_t}} - 1,$$

and therefore, using $\sigma_t^2 = 1 - \alpha_t$,

$$\int_0^t \gamma_t(s) ds = \frac{(1 + \sqrt{\alpha_t})\sqrt{\alpha_t}}{1 - \alpha_t} \left(\frac{1}{\sqrt{\alpha_t}} - 1 \right) = \frac{(1 + \sqrt{\alpha_t})(1 - \sqrt{\alpha_t})}{1 - \alpha_t} = 1.$$

Thus the right-hand side is a convex average of positive-time scores along the probability-flow characteristic. Under continuity of $s \mapsto \nabla \log r_s(\mathbf{z}_s^r)$ at $s = 0$, this average converges to $\nabla \log r(\mathbf{z}_0^r)$ as $t \rightarrow 0$, with the quantitative Gaussian behaviour discussed in Appendix B. \square

A.5 Proof to Proposition 2

Proof. First note that for a fixed decoder $p_\phi(\mathbf{x} | \mathbf{z})$, the optimal encoder distribution associated with the VAE objective is given by

$$q_\phi^*(\mathbf{z} | \mathbf{x}) \propto p_0(\mathbf{z}) \exp\left(\frac{1}{\lambda} \log p_\phi(\mathbf{x} | \mathbf{z})\right).$$

Taking the logarithm and differentiating with respect to \mathbf{z} , we obtain

$$\nabla_{\mathbf{z}} \log q_\phi^*(\mathbf{z} | \mathbf{x}) = \nabla_{\mathbf{z}} \log p_0(\mathbf{z}) + \frac{1}{\lambda} \nabla_{\mathbf{z}} \log p_\phi(\mathbf{x} | \mathbf{z}),$$

and therefore $\nabla_{\mathbf{z}} \log p_\phi(\mathbf{x} | \mathbf{z}) = \lambda \nabla_{\mathbf{z}} \log q_\phi^*(\mathbf{z} | \mathbf{x}) - \lambda \nabla_{\mathbf{z}} \log p_0(\mathbf{z})$. By Fisher's identity,

$$g(\mathbf{z}; \mathbf{y}) = \mathbb{E}_{p_c(\mathbf{x} | \mathbf{y}, \mathbf{z})} [\nabla_{\mathbf{z}} \log p_\phi(\mathbf{x} | \mathbf{z})].$$

Substituting the previous identity into this expression gives

$$g(\mathbf{z}; \mathbf{y}) = \lambda \mathbb{E}_{p_c(\mathbf{x} | \mathbf{y}, \mathbf{z})} [\nabla_{\mathbf{z}} \log q_\phi^*(\mathbf{z} | \mathbf{x})] - \lambda \nabla_{\mathbf{z}} \log p_0(\mathbf{z}).$$

On the other hand, by definition,

$$\hat{g}(\mathbf{z}; \mathbf{y}) := \lambda \mathbb{E}_{p_c(\mathbf{x} | \mathbf{y}, \mathbf{z})} [\nabla_{\mathbf{z}} \log q_\phi(\mathbf{z} | \mathbf{x})] - \lambda \nabla_{\mathbf{z}} \log p_0(\mathbf{z}).$$

Hence,

$$g(\mathbf{z}; \mathbf{y}) - \hat{g}(\mathbf{z}; \mathbf{y}) = \lambda \mathbb{E}_{p_c(\mathbf{x} | \mathbf{y}, \mathbf{z})} [\nabla_{\mathbf{z}} \log q_\phi^*(\mathbf{z} | \mathbf{x}) - \nabla_{\mathbf{z}} \log q_\phi(\mathbf{z} | \mathbf{x})].$$

Taking Euclidean norms and using Jensen's inequality, we obtain

$$\|g(\mathbf{z}; \mathbf{y}) - \hat{g}(\mathbf{z}; \mathbf{y})\|_2^2 \leq \lambda^2 \mathbb{E}_{p_c(\mathbf{x} | \mathbf{y}, \mathbf{z})} [\|\nabla_{\mathbf{z}} \log q_\phi^*(\mathbf{z} | \mathbf{x}) - \nabla_{\mathbf{z}} \log q_\phi(\mathbf{z} | \mathbf{x})\|_2^2].$$

\square

A.6 Proof to the construction of the Gaussian Posterior

Proposition 3. For observation model $p(\mathbf{y} | \mathbf{x}) = \mathcal{N}(\mathbf{y}; \mathbf{A}\mathbf{x}, \sigma_{\mathbf{y}}^2 I)$ and Gaussian decoder $p_{\phi^-}(\mathbf{x} | \mathbf{z}) = \mathcal{N}(\mathbf{x}; \mathcal{D}_{\phi^-}(\mathbf{z}), \sigma_{dec}^2 I)$, we have $p_c(\mathbf{x} | \mathbf{z}, \mathbf{y}) = \mathcal{N}(\mathbf{x}; m(\mathbf{z}), \Sigma)$, where $m(\mathbf{z})$ and Σ are given by:

$$m(\mathbf{z}) = \Sigma (\sigma_{dec}^{-2} \mathcal{D}_{\phi^-}(\mathbf{z}) + \sigma_{\mathbf{y}}^{-2} \mathbf{A}^\top \mathbf{y}), \quad \Sigma = (\sigma_{dec}^{-2} I + \sigma_{\mathbf{y}}^{-2} \mathbf{A}^\top \mathbf{A})^{-1}. \quad (44)$$

Proof. This is the standard conjugate Gaussian update. By Bayes' rule,

$$p_c(\mathbf{x} | \mathbf{z}, \mathbf{y}) \propto p(\mathbf{y} | \mathbf{x}) p_{\phi^-}(\mathbf{x} | \mathbf{z}),$$

and therefore

$$p_c(\mathbf{x}|\mathbf{z}, \mathbf{y}) \propto \exp\left(-\frac{1}{2\sigma_{\mathbf{y}}^2}\|\mathbf{y} - A\mathbf{x}\|_2^2 - \frac{1}{2\sigma_{dec}^2}\|\mathbf{x} - \mathcal{D}_{\phi^-}(\mathbf{z})\|_2^2\right).$$

Expanding the quadratic terms in \mathbf{x} and collecting only the terms that depend on \mathbf{x} , we get

$$\begin{aligned} \log p_c(\mathbf{x}|\mathbf{z}, \mathbf{y}) &= -\frac{1}{2}\mathbf{x}^\top (\sigma_{dec}^{-2}I + \sigma_{\mathbf{y}}^{-2}A^\top A) \mathbf{x} \\ &\quad + \mathbf{x}^\top (\sigma_{dec}^{-2}\mathcal{D}_{\phi^-}(\mathbf{z}) + \sigma_{\mathbf{y}}^{-2}A^\top \mathbf{y}) + \text{const}, \end{aligned}$$

where const does not depend on \mathbf{x} . Define

$$\Sigma^{-1} := \sigma_{dec}^{-2}I + \sigma_{\mathbf{y}}^{-2}A^\top A, \quad m(\mathbf{z}) := \Sigma (\sigma_{dec}^{-2}\mathcal{D}_{\phi^-}(\mathbf{z}) + \sigma_{\mathbf{y}}^{-2}A^\top \mathbf{y}).$$

Since $\sigma_{dec} > 0$, the matrix Σ^{-1} is positive definite and hence invertible. Completing the square gives:

$$\log p_c(\mathbf{x}|\mathbf{z}, \mathbf{y}) = -\frac{1}{2}(\mathbf{x} - m(\mathbf{z}))^\top \Sigma^{-1}(\mathbf{x} - m(\mathbf{z})) + \text{const}.$$

Hence $p_c(\mathbf{x}|\mathbf{z}, \mathbf{y}) = \mathcal{N}(\mathbf{x}; m(\mathbf{z}), \Sigma)$, where Σ and $m(\mathbf{z})$ are defined as above. \square

B Gaussian error analysis for the CM-induced prior score

We provide a closed-form analysis of the CM-induced score surrogate in the Gaussian case. This setting is useful because the clean score, the positive-time score, and the exact probability-flow map are all available explicitly. It also reflects the regime targeted by latent diffusion models, whose VAE latent spaces are regularised toward a standard Gaussian prior.

Let $\mathbf{z}_0 \sim p_0 = \mathcal{N}(0, \Sigma)$ with $\Sigma \succ 0$, and consider the VP forward process $\mathbf{z}_t = \sqrt{\alpha_t}\mathbf{z}_0 + \sigma_t\varepsilon$, where $\varepsilon \sim \mathcal{N}(0, I)$ and $\sigma_t^2 = 1 - \alpha_t$. Then $\mathbf{z}_t \sim p_t = \mathcal{N}(0, M_t)$, with $M_t := \alpha_t\Sigma + \sigma_t^2I = I + \alpha_t(\Sigma - I)$, and the positive-time score is $s_t^*(\mathbf{z}_t) = \nabla_{\mathbf{z}_t} \log p_t(\mathbf{z}_t) = -M_t^{-1}\mathbf{z}_t$. The clean score is $s_0^*(\mathbf{z}_0) = -\Sigma^{-1}\mathbf{z}_0$.

Let g_t^* denote the exact probability-flow map from time t to time 0. Motivated by Proposition 1, we study the normalised CM-induced score

$$\bar{s}_t(\mathbf{z}_t) := (1 + \sqrt{\alpha_t}) \frac{\sqrt{\alpha_t}g_t^*(\mathbf{z}_t) - \mathbf{z}_t}{\sigma_t^2} = \frac{\sqrt{\alpha_t}g_t^*(\mathbf{z}_t) - \mathbf{z}_t}{1 - \sqrt{\alpha_t}}.$$

When $g_\theta = g_t^*$, this is the exact normalised counterpart of the surrogate induced by the CM score formula. In practice, g_t^* is replaced by the consistency model g_θ .

Lemma 3 (Gaussian probability-flow map). *For $p_0 = \mathcal{N}(0, \Sigma)$ and $p_t = \mathcal{N}(0, M_t)$, the exact probability-flow map from time t to time 0 is*

$$g_t^*(\mathbf{z}_t) = \Sigma^{1/2}M_t^{-1/2}\mathbf{z}_t.$$

Proof. Since $M_t = \alpha_t\Sigma + \sigma_t^2I$, the matrices M_t and Σ commute and are diagonalizable in the same orthonormal basis. The linear map $\Sigma^{1/2}M_t^{-1/2}$ transports $\mathcal{N}(0, M_t)$ to $\mathcal{N}(0, \Sigma)$ because

$$\Sigma^{1/2}M_t^{-1/2}M_tM_t^{-1/2}\Sigma^{1/2} = \Sigma.$$

For Gaussian marginals, the probability-flow characteristic is exactly this deterministic Gaussian transport map. \square

We compare $\bar{s}_t(\mathbf{z}_t)$ with the clean score evaluated at the endpoint $g_t^*(\mathbf{z}_t)$, namely $s_0^*(g_t^*(\mathbf{z}_t)) = -\Sigma^{-1}g_t^*(\mathbf{z}_t)$.

Proposition 4 (Gaussian score-surrogate error). *Let $\Sigma = U \text{diag}(\lambda_1, \dots, \lambda_d) U^\top$ and set $m_{t,i} := 1 + \alpha_t(\lambda_i - 1)$. In the eigenbasis of Σ , the i -th coordinate of the error $e_t(\mathbf{z}_t) := \bar{s}_t(\mathbf{z}_t) - s_0^*(g_t^*(\mathbf{z}_t))$ is*

$$(e_t)_i = a_{t,i}(\mathbf{z}_t)_i, \quad a_{t,i} = \frac{1 + \sqrt{\alpha_t}(\lambda_i - 1) - \sqrt{\lambda_i} \sqrt{m_{t,i}}}{\sqrt{\lambda_i}(1 - \sqrt{\alpha_t})\sqrt{m_{t,i}}}.$$

Consequently, for $\mathbf{z}_t \sim \mathcal{N}(0, M_t)$,

$$\mathbb{E}\|e_t(\mathbf{z}_t)\|^2 = \sum_{i=1}^d \frac{[1 + \sqrt{\alpha_t}(\lambda_i - 1) - \sqrt{\lambda_i} \sqrt{m_{t,i}}]^2}{\lambda_i(1 - \sqrt{\alpha_t})^2}.$$

Moreover, $\mathbb{E}\|s_0^*(g_t^*(\mathbf{z}_t))\|^2 = \text{Tr}(\Sigma^{-1}) = \sum_{i=1}^d \lambda_i^{-1}$, so the relative mean-square error is

$$\mathcal{E}_{\text{rel}}(t) = \frac{\sum_{i=1}^d \frac{[1 + \sqrt{\alpha_t}(\lambda_i - 1) - \sqrt{\lambda_i} \sqrt{m_{t,i}}]^2}{\lambda_i(1 - \sqrt{\alpha_t})^2}}{\sum_{i=1}^d \lambda_i^{-1}}.$$

Proof. In the eigenbasis of Σ , Lemma 3 gives $(g_t^*(\mathbf{z}_t))_i = \sqrt{\lambda_i/m_{t,i}}(\mathbf{z}_t)_i$. Hence

$$(\bar{s}_t(\mathbf{z}_t))_i = \frac{\sqrt{\alpha_t} \sqrt{\lambda_i/m_{t,i}} - 1}{1 - \sqrt{\alpha_t}}(\mathbf{z}_t)_i,$$

whereas

$$(s_0^*(g_t^*(\mathbf{z}_t)))_i = -\frac{1}{\lambda_i} \sqrt{\frac{\lambda_i}{m_{t,i}}}(\mathbf{z}_t)_i = -\frac{1}{\sqrt{\lambda_i} \sqrt{m_{t,i}}}(\mathbf{z}_t)_i.$$

Subtracting gives the coefficient $a_{t,i}$. Since $(\mathbf{z}_t)_i \sim \mathcal{N}(0, m_{t,i})$, the mean-square error is obtained by summing $a_{t,i}^2 m_{t,i}$ over the eigen-directions. Finally, since $g_t^*(\mathbf{z}_t) \sim \mathcal{N}(0, \Sigma)$, the clean-score energy is $\mathbb{E}\|\Sigma^{-1} g_t^*(\mathbf{z}_t)\|^2 = \text{Tr}(\Sigma^{-1})$. \square

The expression above immediately shows that the approximation is exact for the VP reference Gaussian. Indeed, if $\Sigma = I$, then $\lambda_i = 1$ and $m_{t,i} = 1$ for every i , so every numerator in Proposition 4 vanishes. Therefore $\bar{s}_t(\mathbf{z}_t) = s_0^*(g_t^*(\mathbf{z}_t))$ for all t .

We also obtain the small-time order of the error.

Corollary 1 (Small-time behaviour). *Assume that the spectrum of Σ is contained in $[\lambda_{\min}, \lambda_{\max}]$ with $\lambda_{\min} > 0$. Then, as $t \rightarrow 0$,*

$$\mathbb{E}\|\bar{s}_t(\mathbf{z}_t) - s_0^*(g_t^*(\mathbf{z}_t))\|^2 = O((1 - \sqrt{\alpha_t})^2) = O(\sigma_t^4).$$

More precisely, in eigen-direction i ,

$$\mathbb{E}[(e_t)_i^2] = \frac{(\lambda_i - 1)^2}{4\lambda_i^3} (1 - \sqrt{\alpha_t})^2 + o((1 - \sqrt{\alpha_t})^2) = \frac{(\lambda_i - 1)^2}{16\lambda_i^3} \sigma_t^4 + o(\sigma_t^4).$$

Proof. Let $\delta_t := 1 - \sqrt{\alpha_t}$. Since $\alpha_t = (1 - \delta_t)^2$, we have $\sigma_t^2 = 2\delta_t - \delta_t^2$. A Taylor expansion gives

$$1 + \sqrt{\alpha_t}(\lambda_i - 1) - \sqrt{\lambda_i} \sqrt{m_{t,i}} = -\frac{\lambda_i - 1}{2\lambda_i} \delta_t^2 + O(\delta_t^3).$$

Substituting this expansion into the exact expression of Proposition 4 yields $\mathbb{E}[(e_t)_i^2] = \frac{(\lambda_i - 1)^2}{4\lambda_i^3} \delta_t^2 + o(\delta_t^2)$. Since $\delta_t = \sigma_t^2 / (1 + \sqrt{\alpha_t})$, this is equivalently $\mathbb{E}[(e_t)_i^2] = \frac{(\lambda_i - 1)^2}{16\lambda_i^3} \sigma_t^4 + o(\sigma_t^4)$. \square

This analysis supports the CM-induced replacement used in the prior subflow. If $g_\theta \simeq g_t^*$, then

$$(1 + \sqrt{\alpha_t}) s_t^{\text{CM}}(\mathbf{z}_t; c) = (1 + \sqrt{\alpha_t}) \frac{\sqrt{\alpha_t} g_\theta(\mathbf{z}_t, t, c) - \mathbf{z}_t}{\sigma_t^2}$$

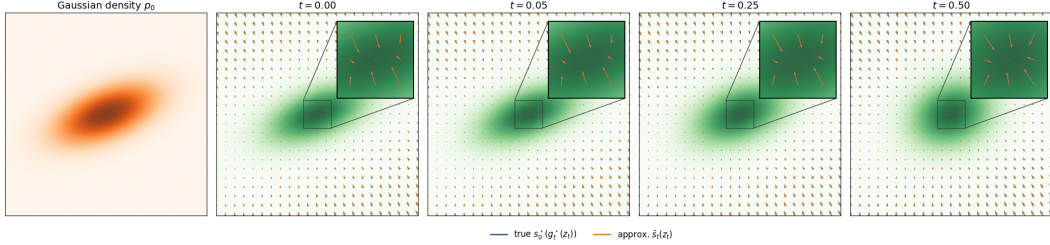


Figure 7: The plots show that, in the Gaussian prior setting, the normalized surrogate tracks the target score well for small and moderate diffusion times. Times $t \in [0, 1]$

approximates the clean prior score evaluated at the reverse-flow endpoint. The approximation is exact for the standard Gaussian prior and its bias scales with the deviation of the covariance eigenvalues λ_i from 1.

This is consistent with the latent spaces used in latent diffusion models. The VAE is trained with a KL regularisation toward a standard Gaussian latent prior, and the latent scaling used by LDMs further encourages approximately whitened latent coordinates. Therefore, when the empirical latent covariance is close to I , the Gaussian calculation predicts a small bias for the CM-induced score surrogate. This provides a simple explanation for the stability of replacing the inaccessible clean prior score by a positive-time CM-induced score in latent-space posterior sampling.

C Algorithm

We now give the pseudocode for simulating the gradient flow. we use the notation \mathbf{z}_k to denote the clean particles, and \mathbf{z}_{t_k} for the ones diffused to the time $t_k \in [0, T]$ and at step $k \in \mathbb{N}$ of the Euler discretization of the ODE.

C.1 Hyperparameters choice

We report the hyperparameters used for both the FFHQ-512 and ImageNet experiments in Table 1. Across all three inverse problems, we use the LCM-LoRA prior [Luo et al. \[2023b\]](#) based on Stable Diffusion 1.5, run CWGF for $K = 16$ iterations, use $N = 1$ particle, enable prompt optimisation, and use cyclic timestep sampling as discussed in Section 4. We set the measurement noise to $\sigma_{\mathbf{y}} = 0.01$, and use the prompt **a photo of a face**. The problem-dependent hyperparameters are reported in Table 3. Here, η_z denotes the particle stepsize, η_c the prompt stepsize, σ_{dec} the decoder standard deviation used in the likelihood approximation, and w_t the timestep-dependent weights used in the prior/likelihood update. The linear weights w_t are defined by $w(t) = 0.1 + 0.8(t/T)$ for $t \in \{999, 879, 759, 639, 499, 379, 259, 139\}$ and $T = 999$. r_c is the radius of the ball centred in the starting prompt c_0 , to which we project every time we apply the prompt update step. Additionally, similar to techniques used in training and distilling diffusion models [[Song et al., 2021a](#), [Kingma and Gao, 2023](#)], we weigh the objective in (20) by the inverse signal-to-noise ratio $W(t) = \sigma_s^2/\alpha_s$ [[Mardani et al., 2024](#), [Wang et al., 2025b](#), [Choi et al., 2026](#)].

Problem	σ_{dec}	η_z	η_c	r_c	w_t
SR $\times 8$	0.25	1.0	0.03	15.0	linear
Gaussian deblur	0.08	1.0	0.66	15.0	linear
Motion deblur	0.05	1.0	0.26	15.0	linear

Table 3: Hyperparameters used for positive-prompt experiments. Common settings are $K = 16$, $N = 1$, 8 LCM timesteps, cyclic timestep sampling, and $\sigma_{\mathbf{y}} = 0.01$.

Algorithm 2. Consistency-regularised Wasserstein Gradient Flow (CWGF)

- 1: **Inputs:** observation \mathbf{y} , forward operator \mathcal{A} , noise level $\sigma_{\mathbf{y}}$, particles $\{\mathbf{z}_0^{(n)}\}_{n=1}^N$, initial prompt c_0 , CM flow map $g_\theta(\cdot, t, c)$, score $s_\theta(\cdot, t; c)$, VAE encoder-decoder $(\mathcal{E}_{\phi^-}, \mathcal{D}_{\phi^-})$, decoder std. σ_{dec} , encoder covariance Σ_{ϕ^-} , VAE weight λ , timestep schedule $t(k)$, weights $w(t)$, stepsizes η_c, η_R, η_L , iterations K .
- 2: Set $\Sigma_{\mathbf{y}} \leftarrow (\sigma_{\text{dec}}^{-2} I + \sigma_{\mathbf{y}}^{-2} A^\top A)^{-1}$.
- 3: **for** $k = 0, \dots, K - 1$ **do**
- 4: Set $t_k \leftarrow t(k)$ and get $\alpha_{t_k}, \sigma_{t_k}$.
- 5: **for** $n = 1, \dots, N$ **do**
- 6: Sample $\varepsilon_k^{(n)} \sim \mathcal{N}(0, I)$ and set $\mathbf{z}_{t_k}^{(n)} \leftarrow \sqrt{\alpha_{t_k}} \mathbf{z}_k^{(n)} + \sigma_{t_k} \varepsilon_k^{(n)}$.
- 7: **end for**
- 8: **Prompt step.** Estimate the prompt gradient by

$$\widehat{\nabla_c \mathcal{R}} \leftarrow \nabla_c \frac{1}{2N} \sum_{n=1}^N w(t_k) \left\| -\frac{\mathbf{z}_{t_k}^{(n)} - \sqrt{\alpha_{t_k}} \mathbf{z}_k^{(n)}}{\sigma_{t_k}^2} - s_\theta(\mathbf{z}_{t_k}^{(n)}, t_k; c_k) \right\|_2^2.$$

- 9: Update $c_{k+1} \leftarrow c_k - \eta_c \widehat{\nabla_c \mathcal{R}}$.
- 10: **Prior subflow.**
- 11: **for** $n = 1, \dots, N$ **do**
- 12: Compute kernel weights

$$\pi_{nm}(t_k) \leftarrow \frac{\exp\left(-\frac{\|\mathbf{z}_{t_k}^{(n)} - \sqrt{\alpha_{t_k}} \mathbf{z}_k^{(m)}\|^2}{2\sigma_{t_k}^2}\right)}{\sum_{j=1}^N \exp\left(-\frac{\|\mathbf{z}_{t_k}^{(n)} - \sqrt{\alpha_{t_k}} \mathbf{z}_k^{(j)}\|^2}{2\sigma_{t_k}^2}\right)}.$$

- 13: Update

$$\bar{\mathbf{z}}_k^{(n)} \leftarrow \mathbf{z}_k^{(n)} + \eta_R \left(g_\theta(\mathbf{z}_{t_k}^{(n)}, t_k, c_k) - \mathbf{z}_k^{(n)} \right) + \eta_R \left(\mathbf{z}_k^{(n)} - \sum_{m=1}^N \pi_{nm}(t_k) \mathbf{z}_k^{(m)} \right).$$

- 14: **end for**
- 15: **Likelihood subflow.**
- 16: **for** $n = 1, \dots, N$ **do**
- 17: Compute the Gaussian pixel-space posterior mean

$$m(\bar{\mathbf{z}}_k^{(n)}) \leftarrow \Sigma_{\mathbf{y}} \left(\sigma_{\text{dec}}^{-2} \mathcal{D}_{\phi^-}(\bar{\mathbf{z}}_k^{(n)}) + \sigma_{\mathbf{y}}^{-2} A^\top \mathbf{y} \right).$$

- 18: Compute the encoder-based likelihood drift

$$\widehat{g}(\bar{\mathbf{z}}_k^{(n)}; \mathbf{y}) \leftarrow \lambda \Sigma_{\phi^-}^{-1} \left(\mathcal{E}_{\phi^-}(m(\bar{\mathbf{z}}_k^{(n)})) - \bar{\mathbf{z}}_k^{(n)} \right) + \lambda \bar{\mathbf{z}}_k^{(n)}.$$

- 19: Update $\mathbf{z}_{k+1}^{(n)} \leftarrow \bar{\mathbf{z}}_k^{(n)} + \eta_L \lambda^{-1} \Sigma_{\phi^-} \widehat{g}(\bar{\mathbf{z}}_k^{(n)}; \mathbf{y})$.
 - 20: **end for**
 - 21: **end for**
 - 22: **return** restored samples $\{\mathcal{D}_{\phi^-}(\mathbf{z}_K^{(n)})\}_{n=1}^N$ and final prompt c_K .
-

For completeness, we also provide in Table 4 the template for the negative-prompt setting, in which the prompt is A photo of a cat.

C.2 Discussion on Related Works

Variational inference for inverse problems. Several works cast posterior sampling with diffusion priors as variational inference, optimizing a tractable family to approximate $p(\mathbf{x} | \mathbf{y})$. A common choice is a Gaussian approximate posterior in pixel space [Mardani et al., 2024], later adapted to latent diffusion priors [Zilberstein et al., 2025]. Other ap-

Problem	σ_{dec}	η_z	η_c	r_c	w_t
SR $\times 8$	0.25	1.0	3.0	15.0	linear
Gaussian deblur	0.08	1.0	3.0	15.0	linear
Motion deblur	0.05	1.0	3.0	15.0	linear

Table 4: Hyperparameters used for the FFHQ-512 negative-prompt experiments with prompt A photo of a cat. Common settings are $K = 16$, $N = 1$, 8 LCM timesteps, cyclic timestep sampling, and $\sigma_y = 0.01$. Here, r_c denotes the prompt projection radius.

proaches parametrise the variational family through denoising distributions or intermediate-time marginals along the diffusion trajectory [Gutha et al., 2025, Janati et al., 2024, Moufad et al., 2025, Zheng et al., 2026]. Our method is most closely related to Wang and Akyildiz [2025], who employ a diffusion model for the prior flow; however, their approach relies on a high NFEs and requires backpropagation through the decoder.

LDMs for inverse problems. Applying LDMs to inverse problems is complicated by the mismatch between latent generation and pixel-space measurements. Many methods enforce data consistency by differentiating through the decoder [Rout et al., 2023, Song et al., 2024, Achituve et al., 2025, Wang and Akyildiz, 2025], while gradient-free alternatives perform pixel-space correction steps (*e.g.* minimising $\|\mathbf{y} - A(\mathbf{x})\|$) followed by re-encoding [Kim et al., 2025a, Spagnoletti et al., 2025b, Shtanchaev et al., 2026]. A complementary direction is to learn a surrogate forward operator directly in latent space [Wang et al., 2025a, Raphaeli et al., 2025]. Our method provides a principled way to incorporate observation information into reconstruction using the encoder, circumventing the need for backpropagation through LDM components

Prompt optimisation in (L)DLMs. Prompt or embedding optimisation has been used both to personalise concepts [Gal et al., 2022, Mokady et al., 2022, Kim et al., 2025b] and to improve test-time generation via text/null-embedding calibration [Wen et al., 2023, Mahajan et al., 2024, Wang et al., 2024, Kim et al., 2025c]. For inverse problems, P2L [Chung et al., 2024] and TReg [Kim et al., 2025a] optimize (positive/negative) text embeddings to better match the observation, while LATINO-PRO [Spagnoletti et al., 2025b] adopts an MMLE perspective and performs online prompt optimisation via SOUL [Bortoli et al., 2020]. Our Euclidean-Wasserstein gradient flow shares a similar MMLE interpretation [Kuntz et al., 2023], but achieves this without requiring nested Langevin steps for sampling.

D Baselines

We briefly recall the main latent-diffusion baselines considered in our comparisons. All methods combine a pretrained LDM prior with a data-consistency correction, but they differ substantially in how the likelihood term is incorporated and how text conditioning is handled.

D.1 LDPS

LDPS is the direct latent-space counterpart of image-domain DPS [Chung et al., 2023]. Let $\hat{\mathbf{z}}_0 := \mathbb{E}[\mathbf{z}_0 \mid \mathbf{z}_t]$ denote the clean latent estimate associated with the current noisy iterate \mathbf{z}_t . The update rule is given by

$$\mathbf{z}_{t-1} = \text{DDIM}(\mathbf{z}_t) - \rho \nabla_{\mathbf{z}_t} \|\mathbf{y} - A\mathcal{D}(\hat{\mathbf{z}}_0)\|_2^2,$$

where ρ denotes the step size and $\text{DDIM}(\cdot)$ represents a single DDIM [Song et al., 2020a] sampling step. In practice, a constant step size $\rho = 1$ is typically used. Thus, LDPS injects the data-fidelity term via a single latent gradient correction applied to the decoded clean estimate.

D.2 PSLD

PSLD [Rout et al., 2023] refines LDPS by adding a latent-manifold stabilization term. In the linear setting, it updates the latent variable by combining a standard DDIM step with two gradient corrections,

$$\mathbf{z}_{t-1} = \text{DDIM}(\mathbf{z}_t) - \rho \nabla_{\mathbf{z}_t} \|\mathbf{y} - A\mathcal{D}(\hat{\mathbf{z}}_0)\|_2^2 - \gamma \nabla_{\mathbf{z}_t} \left\| \hat{\mathbf{z}}_0 - \mathcal{E}\left(A^\top \mathbf{y} + (I - A^\top A)\mathcal{D}(\hat{\mathbf{z}}_0)\right) \right\|_2^2.$$

The first term corresponds to the LDPS correction, while the second encourages the clean latent estimate to remain stable under the decode–project–re-encode cycle. In practice, the method uses a fixed step size $\rho = 1$ together with a regularization weight $\gamma = 0.1$. This additional constraint is designed to keep the iterates close to the natural latent autoencoding manifold.

D.3 P2L

P2L [Chung et al., 2024] alternates between prompt adaptation and latent refinement. At a given diffusion step t , let $\hat{\mathbf{z}}_0(c) := \mathbb{E}[\mathbf{z}_0 \mid \mathbf{z}_t, c]$ denote the current estimate of the clean latent variable conditioned on the text embedding c . The first stage updates the text embedding by approximately maximizing the conditional posterior $p(c \mid \mathbf{z}_t, \mathbf{y})$, leading to the gradient-based update

$$\nabla_c \log p(c \mid \mathbf{z}_t, \mathbf{y}) \approx -\nabla_c \|A\mathcal{D}(\hat{\mathbf{z}}_0(\mathbf{z}_t, c)) - \mathbf{y}\|_2^2,$$

which is typically optimized with Adam [Kingma and Ba, 2014]. Once an updated embedding c_t^* is obtained, the second stage refines the latent variable by approximately maximizing $p(\mathbf{z}_t \mid \mathbf{y}, c_t^*)$ as done by LDPS, i.e.

$$\nabla_{\mathbf{z}_t} \log p(\mathbf{z}_t \mid \mathbf{y}, c_t^*) \approx s_\theta(\mathbf{z}_t, c_t^*) + \rho_t \nabla_{\mathbf{z}_t} \|A\mathcal{D}(\hat{\mathbf{z}}_0(\mathbf{z}_t, c_t^*)) - \mathbf{y}\|_2^2,$$

where $s_\theta(\cdot, c_t^*)$ is the diffusion-model score and ρ_t balances prior and likelihood contributions. Hence, P2L interleaves text-embedding optimization with posterior-guided latent sampling.

D.4 TReg

TReg [Kim et al., 2025a] formulates the reconstruction as an ADMM-style [Boyd et al., 2011] proximal optimization problem in latent space. Given the current clean-latent prediction $\hat{\mathbf{z}}_0$, it considers

$$\min_{\mathbf{x}, \mathbf{z}} \ell_{\text{MAP}}(\mathbf{z}) + \gamma \ell_{\text{TReg}}(\mathbf{z}) \quad \text{s.t.} \quad \mathbf{x} = \mathcal{D}(\mathbf{z}),$$

where

$$\ell_{\text{TReg}}(\mathbf{z}) = \|\mathbf{z} - \hat{\mathbf{z}}_0\|_2^2$$

and the MAP term is

$$\ell_{\text{MAP}}(\mathbf{z}) = -\log p(\mathbf{z} \mid \mathcal{D}(\mathbf{z}), \mathbf{y}) - \log p(\mathbf{y} \mid \mathcal{D}(\mathbf{z})) = \frac{\|\mathbf{z} - \mathcal{E}(\mathcal{D}(\mathbf{z}))\|_2^2}{2\sigma_E^2} + \frac{\|\mathbf{y} - A(\mathcal{D}(\mathbf{z}))\|_2^2}{2\sigma^2}.$$

The method first solves the pixel-space subproblem

$$\hat{\mathbf{x}}_0(\mathbf{y}) = \arg \min_{\mathbf{x}} \frac{\|\mathbf{y} - A(\mathbf{x})\|_2^2}{2\sigma^2} + \lambda \|\mathbf{x} - \mathcal{D}(\hat{\mathbf{z}}_0)\|_2^2,$$

and then updates the latent representation through

$$\hat{\mathbf{z}}_0^{\text{ema}} = \arg \min_{\mathbf{z}} \zeta \|\mathbf{z} - \mathcal{E}(\hat{\mathbf{x}}_0(\mathbf{y}))\|_2^2 + \gamma \|\mathbf{z} - \hat{\mathbf{z}}_0\|_2^2 = \alpha_{t-1} \mathcal{E}(\hat{\mathbf{x}}_0(\mathbf{y})) + (1 - \alpha_{t-1}) \hat{\mathbf{z}}_0,$$

with $\alpha_{t-1} = \zeta / (\zeta + \gamma)$. After this proximal correction, a DDIM step is performed. TReg can additionally adapt the null-text embedding via the so-called *Adaptive Negation* step,

$$c_\emptyset \leftarrow c_\emptyset - \eta \nabla_{c_\emptyset} T_{\text{img}}(\hat{\mathbf{x}}_0(\mathbf{y}), c_\emptyset),$$

where T_{img} denotes the CLIP image encoder [Radford et al., 2021]. This allows the method to preserve a user-provided prompt while still adjusting the unconditional branch used in classifier-free guidance.

D.5 LATINO

LATINO [Spagnoletti et al., 2025b] is a plug-and-play inverse solver that combines a prompt-conditioned latent consistency prior with an exact likelihood correction in pixel space. Given a measurement \mathbf{y} , a prompt embedding c , and a posterior of interest

$$p(\mathbf{x} \mid \mathbf{y}, c) \propto p(\mathbf{y} \mid \mathbf{x}) p(\mathbf{x} \mid c),$$

LATINO may be interpreted as a split-step discretization of an overdamped Langevin dynamics targeting $p(\mathbf{x} \mid \mathbf{y}, c)$: a *prior step* transports the current iterate toward the prompt-conditioned prior by means of the stochastic auto-encoder of Definition 1, and a *likelihood step* enforces data consistency by applying the proximal map associated with $-\log p(\mathbf{y} \mid \mathbf{x})$.

Definition 1 (Stochastic auto-encoder). For a diffusion time $t \in (0, T]$ and a prompt embedding c , we define the stochastic auto-encoder (SAE) associated with the latent consistency prior as the pair $(\mathfrak{E}_t, \mathfrak{D}_{t,c})$, where:

- the stochastic encoder \mathfrak{E}_t maps \mathbf{x} to a noisy latent \mathbf{z}_t according to

$$\mathbf{z}_t \mid \mathbf{x} \sim \mathcal{N}(\sqrt{\alpha_t} \mathcal{E}_{\phi^-}(\mathbf{x}), \sigma_t^2 I), \quad \sigma_t^2 = 1 - \alpha_t,$$

- the stochastic decoder $\mathfrak{D}_{t,c}$ maps \mathbf{z}_t back to image space through

$$\mathfrak{D}_{t,c}(\mathbf{z}_t) := \mathcal{D}_{\phi^-}(\hat{g}_{\theta^-}(\mathbf{z}_t, t, c)).$$

Equivalently, the associated prior transport on image space is the Markov kernel

$$\mathbf{x} \mapsto \mathfrak{D}_{t,c} \circ \mathfrak{E}_t(\mathbf{x}).$$

More precisely, starting from the current image iterate $\mathbf{x}^{(k-1)}$, LATINO first maps it to latent space and perturbs it at diffusion time t_k ,

$$\mathbf{z}_{t_k}^{(k)} = \sqrt{\alpha_{t_k}} \mathcal{E}_{\phi^-}(\mathbf{x}^{(k-1)}) + \sigma_{t_k} \epsilon^{(k)}, \quad \epsilon^{(k)} \sim \mathcal{N}(0, I).$$

The latent consistency model then predicts a cleaned latent

$$\hat{\mathbf{z}}_0^{(k)} = \hat{g}_{\theta^-}(\mathbf{z}_{t_k}^{(k)}, t_k, c),$$

which is decoded back to pixel space as

$$\mathbf{u}^{(k)} = \mathcal{D}_{\phi^-}(\hat{\mathbf{z}}_0^{(k)}) = \mathfrak{D}_{t_k,c}(\mathbf{z}_{t_k}^{(k)}).$$

Finally, the measurement model is enforced through the proximal correction

$$\mathbf{x}^{(k)} = \text{prox}_{\delta_k g_y}(\mathbf{u}^{(k)}), \quad g_y(\mathbf{x}) := -\log p(\mathbf{y} \mid \mathbf{x}),$$

where $\delta_k > 0$ is an iteration-dependent parameter balancing the prior and likelihood contributions. The full method is described in Algorithm 3.

Algorithm 3. LATINO

- 1: **Input:** measurement \mathbf{y} , prompt embedding c , initialisation $\mathbf{x}^{(0)} = \mathcal{A}^\dagger \mathbf{y}$, number of steps K , schedules $\{t_k\}_{k=1}^K$ and $\{\delta_k\}_{k=1}^K$
 - 2: **for** $k = 1, \dots, K$ **do**
 - 3: Sample $\epsilon^{(k)} \sim \mathcal{N}(0, I)$
 - 4: $\mathbf{z}_{t_k}^{(k)} \leftarrow \sqrt{\alpha_{t_k}} \mathcal{E}_{\phi^-}(\mathbf{x}^{(k-1)}) + \sigma_{t_k} \epsilon^{(k)}$
 - 5: $\mathbf{u}^{(k)} \leftarrow \mathcal{D}_{\phi^-}(\hat{g}_{\theta^-}(\mathbf{z}_{t_k}^{(k)}, t_k, c))$
 - 6: $\mathbf{x}^{(k)} \leftarrow \text{prox}_{\delta_k g_y}(\mathbf{u}^{(k)})$
 - 7: **end for**
 - 8: **return** $\mathbf{x}^{(K)}$
-

In practice, the algorithm is warm-started from $\mathcal{A}^\dagger \mathbf{y}$ and uses an annealed schedule $\{(t_k, \delta_k)\}_{k=1}^K$, with decreasing diffusion times and task-dependent proximal strengths.

D.6 LATINO-PRO

LATINO-PRO extends LATINO by treating the prompt embedding c as an unknown parameter to be estimated from the observation. Rather than fixing c a priori, it adopts a maximum marginal likelihood estimation (MML) strategy and seeks

$$\hat{c}(\mathbf{y}) \in \arg \max_c p(\mathbf{y} | c), \quad p(\mathbf{y} | c) = \int p(\mathbf{y} | \mathbf{x}) p(\mathbf{x} | c) d\mathbf{x}.$$

The optimized prompt is then used to sample from the empirical-Bayes posterior $p(\mathbf{x} | \mathbf{y}, \hat{c}(\mathbf{y}))$. Through Fisher’s identity we get

$$\nabla_c \log p(\mathbf{y} | c) = \mathbb{E}_{p(\mathbf{x} | \mathbf{y}, c)} [\nabla_c \log p(\mathbf{x} | c)],$$

which shows that the marginal-likelihood gradient can be approximated by posterior samples. LATINO-PRO therefore alternates between:

1. running a short LATINO chain targeting $p(\mathbf{x} | \mathbf{y}, c_m)$, starting from the current state and using the current prompt c_m ;
2. updating the prompt embedding through a stochastic approximation proximal gradient (SAPG) step,

$$c_{m+1} = \Pi_{\mathcal{C}}(c_m + \gamma_m h_m),$$

where $\gamma_m > 0$ is a stepsize, $\Pi_{\mathcal{C}}$ denotes projection onto an admissible set \mathcal{C} , and h_m is a Monte Carlo approximation of $\nabla_c \log p(\mathbf{y} | c_m)$.

In the LATINO-PRO implementation, the gradient estimator is computed in latent space by differentiating the transition densities induced by the stochastic latent auto-encoding recursion. Concretely, after generating latent states

$$\{\mathbf{z}_{t_1}^{(1)}, \dots, \mathbf{z}_{t_{N_m}}^{(N_m)}\}$$

along a short LATINO trajectory (i.e. using $N_m \sim K/2$ steps), one uses the approximation

$$h_m \approx \nabla_c \log p\left(\mathbf{z}_{t_1}^{(1)}, \dots, \mathbf{z}_{t_{N_m}}^{(N_m)} | c_m\right),$$

which can be evaluated using automatic differentiation via the latent consistency model (see [Spagnoletti et al., 2025b][Appendix A] for details). Similar to CWGF, the prompt update acts in latent space and avoids differentiating through the full pixel-space proximal correction.

Overall, LATINO-PRO may thus be viewed as an alternating scheme:

$$\text{short posterior sampling with LATINO} \longrightarrow \text{prompt update by SAPG} \longrightarrow \text{repeat}.$$

After a small number of such outer iterations, one obtains an optimized prompt embedding $\hat{c}(\mathbf{y})$, and a final LATINO pass can then be run with this calibrated prompt to produce a higher-quality reconstruction.

E Enhanced sampling variability on MNIST

While the CWGF algorithm has proven to be SOTA on multiple image restoration tasks, the ablation study in Appendix G shows how a single particle is enough to approximate $\mu(\mathbf{z} | \mathbf{y})$ for the sake of the restoration task (i.e. that the metrics do not seem to improve when $N > 1$). This phenomenon seems counterintuitive, but it is actually explainable as the latent space of our SD1.5-based LCM is too big to appreciate significant interactions between particles when $N < 10$ as in our experiments. Indeed, as clarified in Section 3.1, when $N > 1$ in (19) we get an extra interaction term $\mathbf{z}_0^{(i)} - \sum_{j=1}^N \pi_{ij}(s) \mathbf{z}_0^{(j)}$, where π_{ij} can be read as a similarity matrix between the different particles at level of noise s . Thus, when the particles are too similar (and we would like to enhance the differences), this extra term pushes away from the pondered mean, while a diagonal $\pi_{ij} \sim \text{Id}$ annihilates the term, and the algorithm follows, i.e. as LATINO would do, on N samples in parallel. Thus, observing

$\pi_{ij} \sim \text{Id}$, as in our experiments, indicates that the particles are already sufficiently distinct to require only limited reshuffling during sampling.

The situation may be different when the space in which the particles $\{z^{(i)}\}_i$ live is much smaller. To illustrate this different scenario, we trained a small LCM on the MNIST dataset [Deng, 2012], and, to further reduce the dimensionality of the latent space, we embedded the samples in the latent space of a VAE with $d = 10$ dimensions. The training of the VAE ($\mathcal{D}_{\phi^-}, \mathcal{E}_{\phi^-}$) followed [Dubois et al., 2019, Bickford Smith et al., 2024], while the training of the LCM is inspired by [Lu and Song, 2025], for which the timesteps are normalised to be $\in [0, \pi/2]$. The implementation uses CWGF (no prompt opt.) following Algorithm 2, since the LCM is unconditional in this scenario. Concerning the inverse problem considered, we define a simple inpainting with a central mask of shape 16×16 , while $\sigma_y = 0.01$. Other hyperparameters are set: $K = 8$, s takes 4 equi-spaced values in the Karras [Karras et al., 2022] time schedule (so we cycle through them, and we use only the first two for $k > 4$), $\mathbf{1r}_z = 0.5$, $w_t = 0.5$, $\sigma_{dec} = 0.6$.

We then proceed in solving $\mathbf{y} = \mathcal{A}\mathbf{x} + \mathbf{n}$ on a sample \mathbf{x} from the MNIST test set, and we compare two ways of doing so: (i) sampling $M = 1024$ particles from $p(\mathbf{x} | \mathbf{y})$ with CWGF (no prompt opt.) in parallel, meaning that $N = M = 1024$, or (ii) repeating M times the CWGF (no prompt opt.) scheme for $N = 1$.

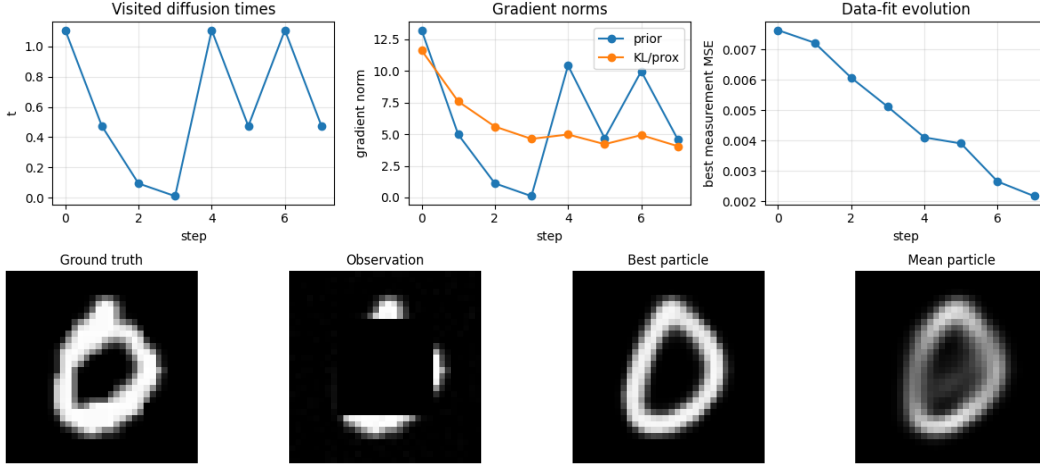


Figure 8: **MNIST box inpainting with CWGF (no prompt opt.)**. *Top*: visited diffusion times $t(k) \in [0, \pi/2]$, gradient norms (prior vs. likelihood/prox), and evolution of the best data-fit over iterations. *Bottom*: ground truth, blurred measurement, best particle, and particle mean at the final iteration.

We report the sampling dynamics and a representative reconstruction in Figure 8, confirming that the reconstruction runs successfully. To isolate the role of particle interactions, Figure 9 compares joint evolution ($N = M$) against M independent runs ($N = 1$). A visual analysis of the samples shows greater variability in the $M = N$ case (i.e. “all at once”), as expected from the discussion of the repulsive term. Figure 10 summarizes the resulting diversity in latent space and reconstruction quality, confirming the visual insights. Indeed, the first two Principal Components in the latent space show a more extensive coverage for the $M = N$ setting, proving a *repulsion off the mean* phenomenon. Similarly, the PSNR histogram for this case shows a larger support and reaches a higher maximum PSNR. Finally, we trained a small classifier on the MNIST training dataset (achieving $\sim 98\%$ accuracy on the test set) to detect the digit distribution in the two cases. In Figure 11a, we observe a wider number of classes retrieved when the algorithm samples in parallel the 1024 particles. Indeed, in the “batched” case, we do not observe any digit labelled as 5, while, as observed in Figure 11b, it is a plausible solution to the inpainting problem, and we observe these cases when $M = N$.

Most importantly, we have experimental evidence that the matrix π_{ij} does not collapse to Id except when s is close to 0, as shown in Figure 12, where we plot the first 4 iterations within CWGF (no prompt opt.) for $N = 20$ particles.

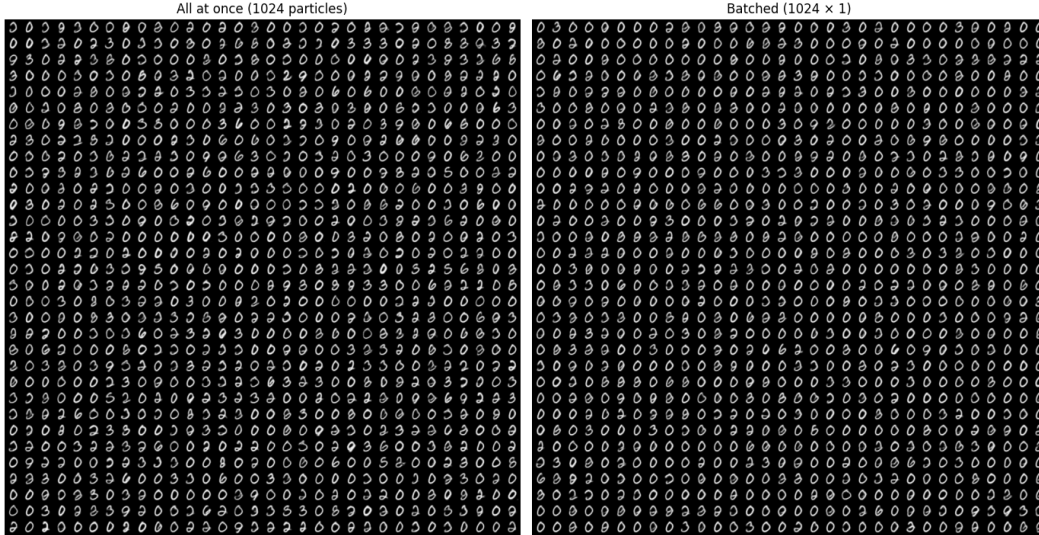


Figure 9: **Effect of particle interactions.** Samples obtained with $M = 1024$ posterior draws using (left) CWGF (no prompt opt.) with $N = M$ particles evolved jointly, versus (right) M independent runs with $N = 1$ (no interaction term).

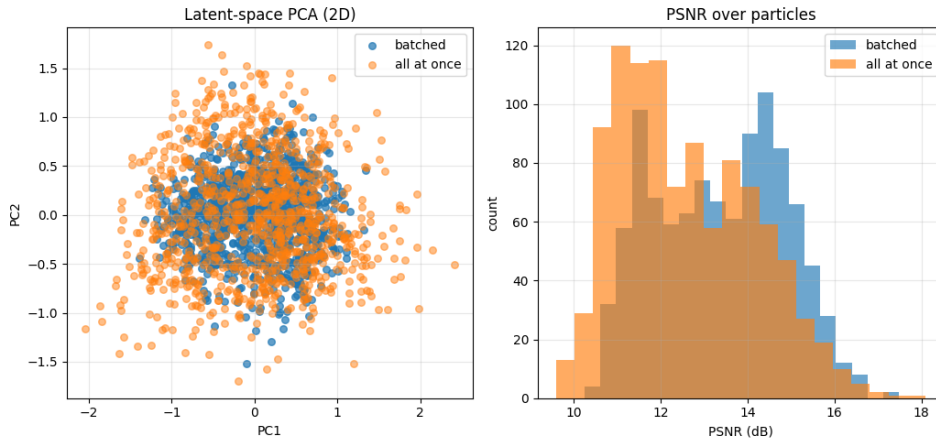


Figure 10: **Distributional comparison of posterior samples.** *Left:* 2D PCA of latent samples, contrasting joint evolution ($N = M$) against independent runs ($N = 1$ repeated). *Right:* histogram of PSNR across the $M = 1024$ samples for the two regimes.

We can then conclude that, in smaller latent spaces where the particles actually interact, the posterior reconstructions show a larger variability, allowing for non-obvious solutions that lie on the tails of the posterior distribution $p(\mathbf{x}|\mathbf{y})$. We encourage future research to exploit this feature of the CWGF algorithm in contexts and applications where it is important to correctly sample the tail of the considered conditional distribution.

F Non-linear problems

In addition to the linear Gaussian inverse problems considered in our theory, we also evaluate a more challenging *nonlinear* restoration task based on JPEG compression. Given a clean image $\mathbf{x}_0 \in \mathcal{X}$, we generate the observation as

$$\mathbf{y} = \mathcal{J}_q(\mathbf{x}_0 + \eta_0) + \mathbf{n}, \quad \eta_0 \sim \mathcal{N}(0, \sigma_{\mathbf{x}_0}^2 I), \quad \mathbf{n} \sim \mathcal{N}(0, \sigma_{\mathbf{y}}^2 I), \quad (45)$$

where \mathcal{J}_q denotes JPEG compression–decompression at quality factor q . This setting departs from the assumptions of (1), since \mathcal{J}_q is nonlinear and non-differentiable due to quantization, so the closed-form Gaussian posterior and the associated linear proximal operator are

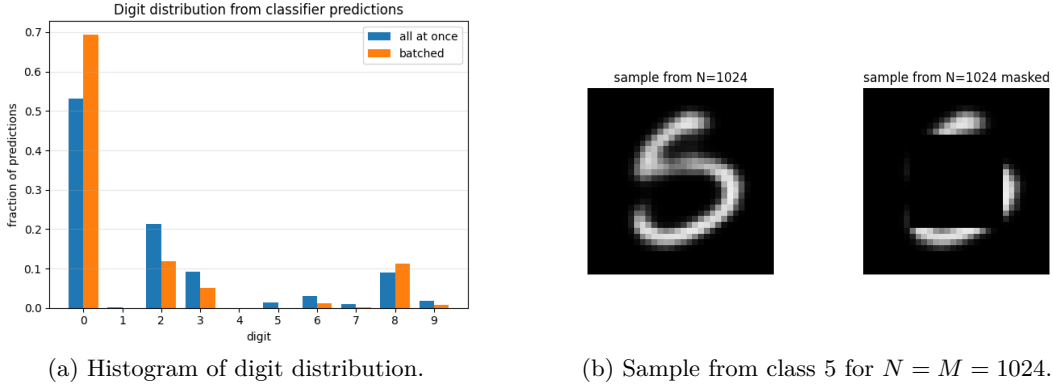


Figure 11: Classification of posterior samples.

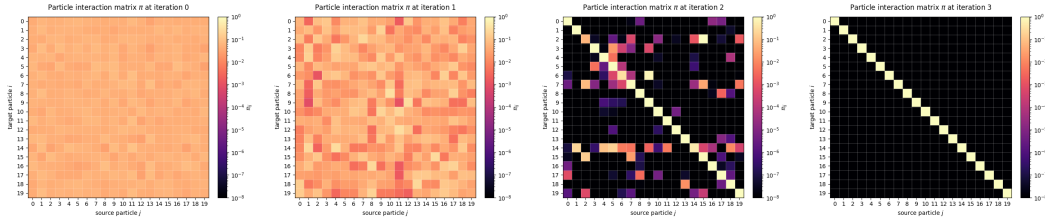


Figure 12: Evolution of the particle interaction matrix π . Heatmaps of π_{ij} at iterations $k = 0, 1, 2, 3$ (left to right).

no longer available. In practice, we keep the same posterior-guided sampling scheme and replace the exact data-consistency step by an approximate proximal update based on the deterministic surrogate $\mathcal{A}_{\text{det}}(\mathbf{x}) = \mathcal{J}_q(\mathbf{x})$, while treating the stochastic perturbations η_0 and \mathbf{n} as part of the observed measurement. More precisely, at each iteration we approximately solve

$$\mu(\mathbf{z}) \approx \arg \min_{\mathbf{u} \in X} \frac{1}{2} \|\mathbf{u} - \mathbf{x}\|_2^2 + \frac{\sigma_{dec}^2}{2\sigma_y^2} \|\mathcal{A}_{\text{det}}(\mathbf{u}) - \mathbf{y}\|_2^2. \quad (46)$$

by a small number of projected gradient steps, using the identity as a practical approximation of the adjoint of \mathcal{A}_{det} . This provides a simple and effective way to assess the robustness of our method beyond the strictly linear regime.

Table 5 and Figure 13 show results on the FFHQ dataset when JPEG quality level is set to $q = 20\%$, $\sigma_{x_0} = 0.05$, and $\sigma_y = 0.01$.

Method	NFE↓	Noisy JPEG		
		FID↓	PSNR↑	LPIPS↓
LATINO	8	34.91	25.87	0.448
LATINO-PRO	65	<u>33.45</u>	<u>26.28</u>	<u>0.433</u>
P2L	400	75.57	18.28	0.529
TReg	200	94.42	20.04	0.703
CWGF	<u>16</u>	30.71	26.33	0.355

Table 5: Results on Noisy JPEG, all with noise $\sigma_y = 0.01$ on the FFHQ-512 val dataset. Prompt: A photo of a face. **Bold**: best, underline: second best.

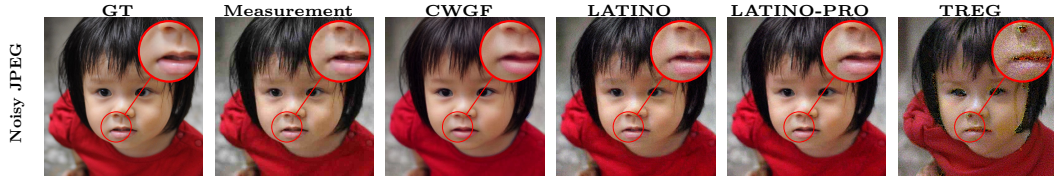


Figure 13: Qualitative comparison of image restoration results for the non-linear problems considered. Samples taken from FFHQ-512. Prompt: A photo of a face.

G Ablations

G.1 Ablation on Prompt Optimisation

We perform ablations on the effect of prompt optimisation under the same hyperparameters as in Appendix C.1. The results are shown in Tables 6, 7, and 8 for Gaussian deblurring, motion deblurring, and SR \times 8, respectively. We observe that prompt optimisation consistently improves the performance of the adversarial prompt, while it has less of an effect on the positive prompt, possibly due to the fact that the prompt is already well-aligned with the observations.

Setting	Prompt opt.	FID \downarrow	LPIPS \downarrow	PSNR \uparrow
Positive prompt	\times	21.28	0.306	29.37
Positive prompt	\checkmark	21.95	0.306	29.23
Adversarial prompt	\times	32.91	0.354	28.64
Adversarial prompt	\checkmark	27.58	0.322	29.59

Table 6: Prompt ablation study on Gaussian deblurring.

Setting	Prompt opt.	FID \downarrow	LPIPS \downarrow	PSNR \uparrow
Positive prompt	\times	23.12	0.338	27.83
Positive prompt	\checkmark	23.03	0.338	27.82
Adversarial prompt	\times	32.20	0.357	27.86
Adversarial prompt	\checkmark	25.99	0.339	28.16

Table 7: Prompt ablation study on motion deblurring.

G.2 Ablation on Weights w_t

We provide a sensitivity analysis of CWGF to the step weighting $w(t)$ used in implementation. The weight $w(t)$ controls the strength of the prior-flow correction at each diffusion timestep. Specifically, we set $w(t)$ to be constant in t and vary it in $[0.1, 1.0]$ (Figure 14) to isolate the effect of its overall scale. The other hyperparameters are the same as in Appendix C.1.

G.3 Ablation on Prompt Learning Rate η_c

Similarly we provide a sensitivity analysis of CWGF to the prompt learning rate in the positive and adversarial prompt settings. The other hyperparameters are the same as in Appendix C.1. We vary η_c in $[0.01, 1.0]$ for the positive prompt (Figure 15) and in $[0.01, 10.0]$ for the adversarial prompt (Figure 16). As shown in the figures, CWGF has a preference for smaller learning rates in the positive prompt setting.

G.4 Ablation on Timestep Sampling

We now provide an ablation study on different timestep sampling strategies used for our score approximation in Section 3.1 to isolate the effect of the timestep ordering.

Setting	Prompt opt.	FID ↓	LPIPS ↓	PSNR ↑
Positive prompt	✗	35.67	0.373	26.97
Positive prompt	✓	35.52	0.372	26.95
Adversarial prompt	✗	92.43	0.456	26.24
Adversarial prompt	✓	50.07	0.415	27.39

Table 8: Prompt ablation study on SR×8.

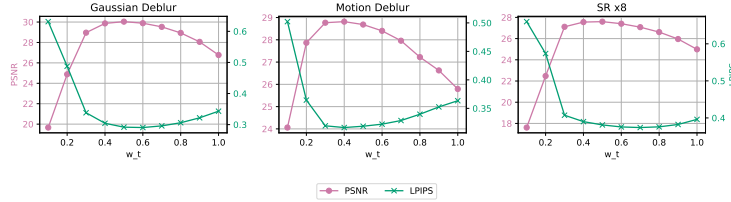


Figure 14: Sensitivity of CWGF to w_t measured in PSNR and LPIPS averaged over 50 held-out images on FFHQ512.

We compare our cyclic timestep sampling with uniform sampling $t(k) \sim \text{Unif}(\mathcal{T})$ for $\mathcal{T} = \{999, 879, 759, 639, 499, 379, 259, 139\}$ and a decreasing schedule that repeats each element of \mathcal{T} consecutively *i.e.* $\{999, 999, \dots, 259, 259, 139, 139\}$. We present the results for the positive prompt in Table 9 and the adversarial prompt in Table 10. We note that uniform sampling performs worse than the other two strategies, aligning with the fact that the $t(k)$ used in approximating the score acts as an annealing parameter for coarse-to-fine refinement.

G.5 Ablation on Particle Count N

We now provide an ablation study on the number of particles N used in CWGF in the high dimensional setting on the FFHQ 512 dataset. We vary N in $\{1, 4, 8\}$ and present the results for the positive and adversarial prompts in Table 11 and Table 12, respectively. We evaluate the performance of multi-particle versions of CWGF by randomly selecting one of the N particles at the end of the algorithm to compute the metrics. While we note that the improvements are only marginal, this may be due to the high dimensional latent space. We refer to Appendix E for a more detailed analysis on the effect of N in a lower dimensional setting.

G.6 Ablation on Prompt Optimisation Score

We now discuss whether the LCM score is a good proxy for the teacher score in prompt optimisation via (21). We compare the performance of CWGF when using the LCM score and the teacher score in prompt optimisation; when using the teacher score, we scale the prompt gradient to ensure it has the same norm as the LCM’s prompt gradient. We present the results for the positive and adversarial prompts in Table 13 and Table 14, respectively. Additionally, we plot in Figure 17 the cosine similarity values between the LCM score and the teacher score across diffusion times during CWGF computed over 50 held-out images. We note that the LCM score aligns well with the teacher score, suggesting the scale mismatch

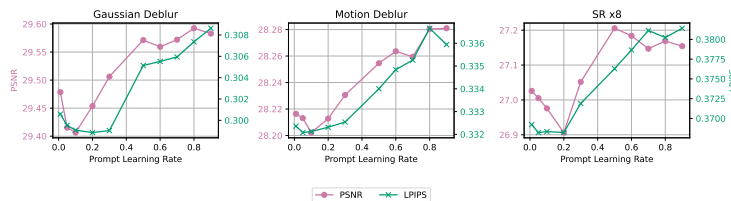


Figure 15: Sensitivity of CWGF to η_c measured in PSNR and LPIPS averaged over 50 held-out images on FFHQ512. Using positive prompt: A photo of a face.

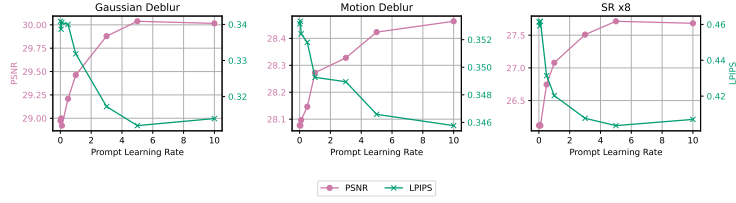


Figure 16: Sensitivity of CWGF to η_c measured in PSNR and LPIPS averaged over 50 held-out images on FFHQ512. Using adversarial prompt: A photo of a cat.

Method	Gaussian Deblur			Motion Deblur			SR $\times 8$		
	FID \downarrow	PSNR \uparrow	LPIPS \downarrow	FID \downarrow	PSNR \uparrow	LPIPS \downarrow	FID \downarrow	PSNR \uparrow	LPIPS \downarrow
Uniform	24.77	29.47	0.323	27.33	27.98	0.348	48.44	27.29	0.403
Decreasing	22.63	29.57	0.315	22.93	28.13	0.338	34.50	27.00	0.367
Cyclic	21.95	29.42	0.309	23.18	27.98	0.338	35.52	26.95	0.372

Table 9: Ablation on the timestep sampling on FFHQ 512 using positive prompt: A photo of a face.

Method	Gaussian Deblur			Motion Deblur			SR $\times 8$		
	FID \downarrow	PSNR \uparrow	LPIPS \downarrow	FID \downarrow	PSNR \uparrow	LPIPS \downarrow	FID \downarrow	PSNR \uparrow	LPIPS \downarrow
Uniform	26.09	29.49	0.338	29.91	27.93	0.361	55.82	27.31	0.432
Decreasing	25.46	29.79	0.320	25.60	28.27	0.349	50.39	27.53	0.410
Cyclic	27.58	29.59	0.322	25.99	28.16	0.339	50.07	27.39	0.415

Table 10: Ablation on the timestep sampling on FFHQ 512 using adversarial prompt: A photo of a cat.

Method	Gaussian Deblur			Motion Deblur			SR $\times 8$		
	FID \downarrow	PSNR \uparrow	LPIPS \downarrow	FID \downarrow	PSNR \uparrow	LPIPS \downarrow	FID \downarrow	PSNR \uparrow	LPIPS \downarrow
N=1	21.95	29.42	0.309	23.18	27.98	0.338	35.52	26.95	0.372
N=4	21.53	29.31	0.307	23.22	27.93	0.337	35.28	26.94	0.371
N=8	21.45	29.27	0.306	23.10	27.93	0.336	35.16	26.94	0.370

Table 11: Ablation on the number of particles N on FFHQ 512 using positive prompt: A photo of a face.

Method	Gaussian Deblur			Motion Deblur			SR $\times 8$		
	FID \downarrow	PSNR \uparrow	LPIPS \downarrow	FID \downarrow	PSNR \uparrow	LPIPS \downarrow	FID \downarrow	PSNR \uparrow	LPIPS \downarrow
N=1	27.58	29.59	0.322	25.99	28.16	0.339	50.07	27.39	0.415
N=4	25.68	29.66	0.319	26.45	28.18	0.351	52.02	27.44	0.411
N=8	26.35	29.66	0.317	26.52	28.19	0.351	52.55	27.42	0.411

Table 12: Ablation on the number of particles N on FFHQ 512 using adversarial prompt: A photo of a cat.

between the LCM and teacher parametrisations, likely due to differences in classifier-free guidance parametrisation during LCM training [Luo et al., 2023a]; we leave a more detailed analysis of this for future work.

Method	Gaussian Deblur			Motion Deblur			SR $\times 8$		
	FID \downarrow	PSNR \uparrow	LPIPS \downarrow	FID \downarrow	PSNR \uparrow	LPIPS \downarrow	FID \downarrow	PSNR \uparrow	LPIPS \downarrow
Teacher score (SD1.5)	21.97	29.43	0.319	23.36	28.00	0.340	36.19	27.04	0.371
LCM score	21.95	29.42	0.309	23.18	27.98	0.338	35.52	26.95	0.372

Table 13: Ablation on the use of teacher score in prompt optimisation on FFHQ 512 using positive prompt: **A photo of a face.**

Method	Gaussian Deblur			Motion Deblur			SR $\times 8$		
	FID \downarrow	PSNR \uparrow	LPIPS \downarrow	FID \downarrow	PSNR \uparrow	LPIPS \downarrow	FID \downarrow	PSNR \uparrow	LPIPS \downarrow
Teacher score (SD1.5)	23.00	29.36	0.328	24.87	27.85	0.350	48.28	26.94	0.412
LCM score	27.58	29.59	0.322	25.99	28.16	0.339	50.07	27.39	0.415

Table 14: Ablation on the use of teacher score in prompt optimisation on FFHQ 512 using adversarial prompt: **A photo of a cat.**

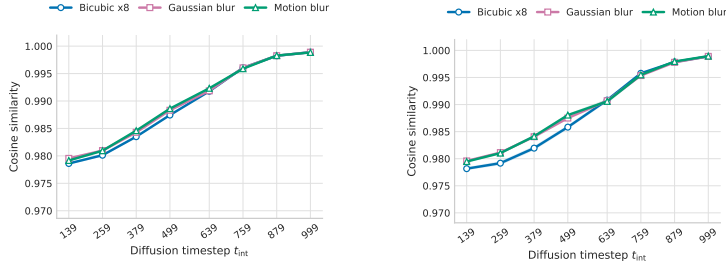


Figure 17: Cosine similarity between the teacher and LCM score estimate. Left: positive prompt. Right: adversarial prompt.

H Computational Resources

For all experiments, we use NVIDIA GPUs on internal HPCs, which include a mixture of A40, L40S, RTX A6000, and GH200s. However, we also point out that our method can run on consumer GPUs. Table 15 shows the memory footprint and runtime of our method, compared to those of the baselines, computed on the same machine.

Method	VRAM (GB)	Time (s)	Resolution
CWGF	8.66	8.72	512 ²
LATINO	4.16	2.89	512 ²
LATINO-PRO	9.27	32.3	512 ²
TReg	~6.40	40.5	512 ²
P2L	~10.6	600	512 ²
LDPS	9.51	176	512 ²
PSLD	10.3	185	512 ²

Table 15: Runtime and memory comparisons.

I Additional samples

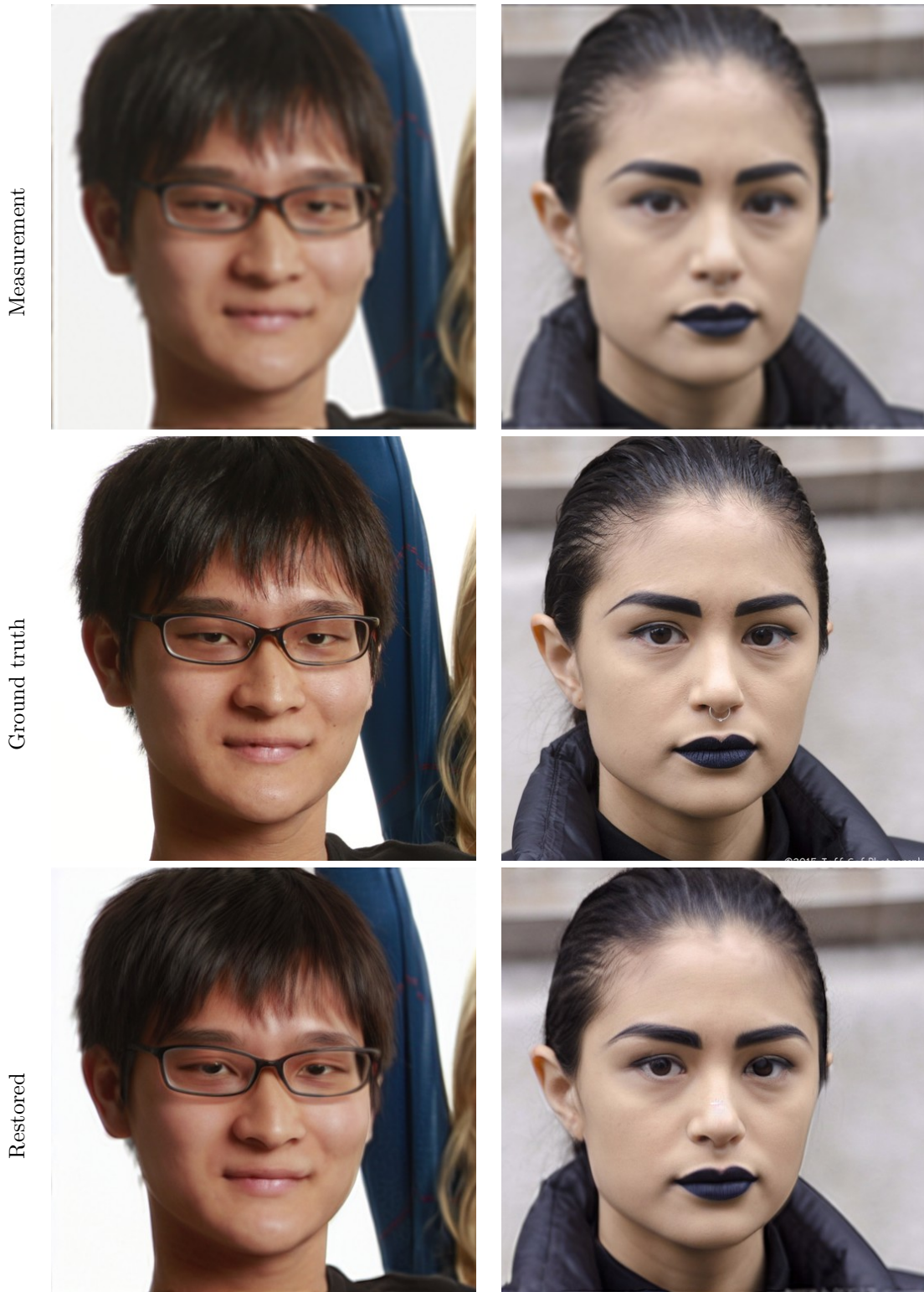


Figure 18: Gaussian deblur FFHQ-512 CWGF.

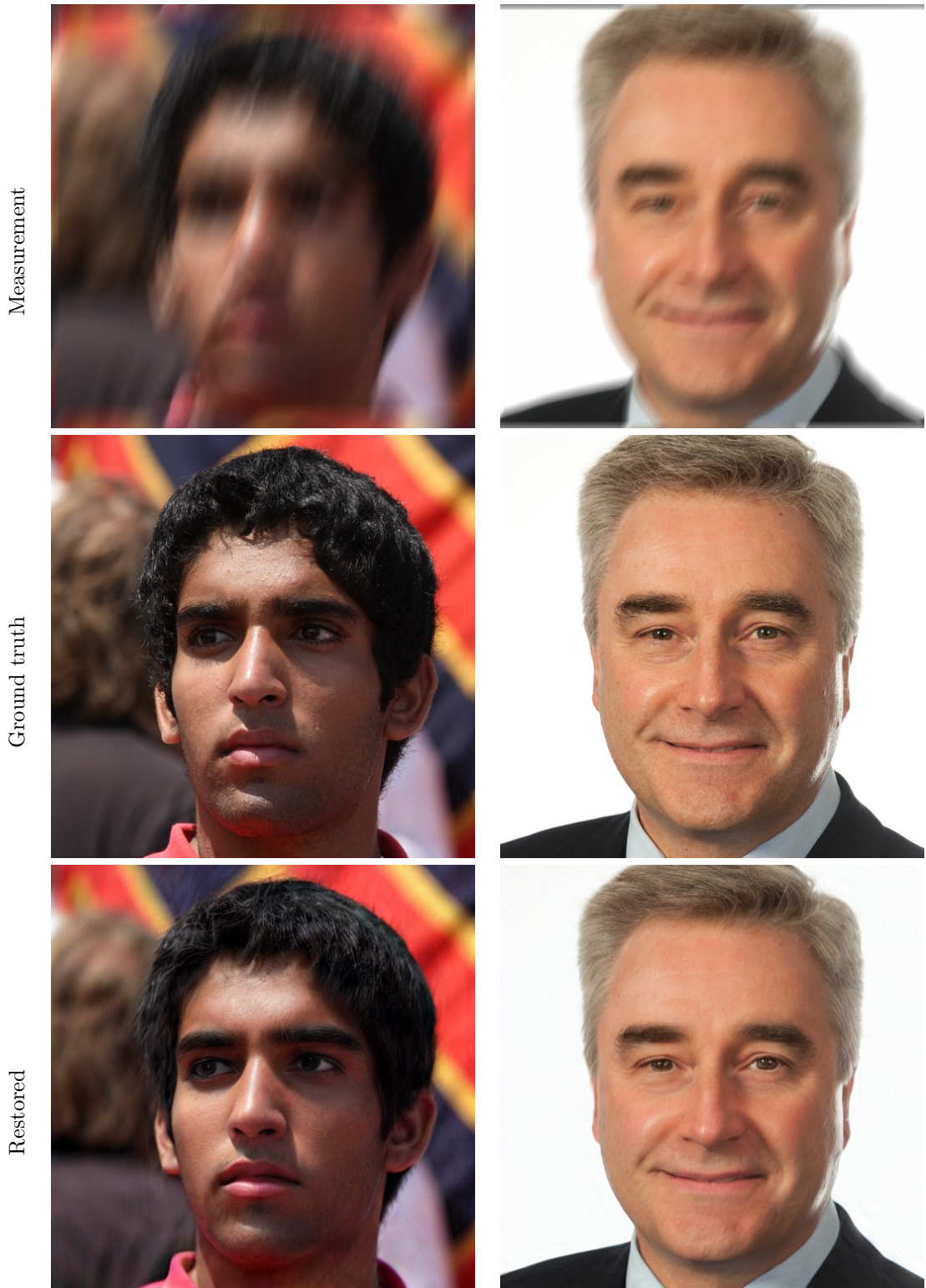


Figure 19: Motion deblur FFHQ-512 CWGF.



Figure 20: SR \times 8 FFHQ-512 CWGF.